# STARS

2018

# Theoretical Paschen's Law Model for Aerospace Vehicles: Validation Experiment

Jaysen Mulligan Aroche
*University of Central Florida*

## STARS Citation

Mulligan Aroche, Jaysen, "Theoretical Paschen's Law Model for Aerospace Vehicles: Validation Experiment" (2018). *Electronic Theses and Dissertations, 2004-2019*. 5822.
https://stars.library.ucf.edu/etd/5822

THEORETICAL PASCHEN'S LAW MODEL FOR
AEROSPACE VEHICLES: VALIDATION EXPERIMENT


by


JAYSEN MULLIGAN AROCHE
B.S. University of Central Florida, 2016


A thesis submitted in partial fulfillment of the requirements
for the degree of Master of Science
in the Department of Mechanical and Aerospace Engineering
in the College of Engineering and Computer Science
at the University of Central Florida
Orlando, Florida


Spring Term
2018

# ABSTRACT

Aerospace vehicles often experience triboelectric charging while traversing the atmosphere. Triboelectric charging occurs when a material come into frictional contact with a different material. Aerospace vehicles triboelectrically charge due to frictional contact with dust and ice crystals suspended in the atmosphere. Launch vehicles traversing ice clouds in low-pressure atmosphere are especially prone to electrostatic discharge events (i.e. sparks). These conditions are hazardous and affect the vehicle's launch commit criteria. In 2010, engineers from an ARES-I rocket launch reported concerns with triboelectric charging over their self-destruct system antenna. This concern was addressed by putting the antenna through harsh conditions in a laboratory environment. The need for laboratory testing could have been avoided if there was a mathematical model to predict these events. These discharge events can typically be predicted by the Classical Paschen's Law, which relates discharge voltage to pressure, material and distance between the charged and ground surfaces (i.e. electrodes). However, the Classical Paschen's Law does not capture any aerodynamic considerations such as large bulk flow and compressibility effects. It became apparent that a new model would be needed to predict a discharge voltage with aerodynamic considerations. This research focused on defining a theoretical model and providing experimental data to validate the model. The hypothesis of this work is that charged ions are removed too quickly for enough charge to build up and result in an electrostatic discharge at the voltage that is predicted by the Classical Paschen's Law. The wind tunnel testing for this experiment was conducted at the Center for Advanced Turbomachinery & Energy Research (CATER) facility. A charged electrode was exposed to flows at Mach numbers 1.5 to 3.5. It was found that the supersonic flow suppressed the electrostatic discharge events. The voltage required

for an electrostatic discharge at supersonic conditions increased by a factor of three. The modified

Paschen's Law can help in defining the launch commit criteria of aerospace vehicles.

# TABLE OF CONTENTS

# LIST OF FIGURES

# LIST OF TABLES

# CHAPTER 1: INTRODUCTION

## 1.1 <u>Introduction</u>

This purpose of this work was to provide data for the validation of a theoretical model of the Classical Paschen's Law that considered an aerodynamic component. The need for such a theoretical model was uncovered during a triboelectric induced electrostatic discharge event investigation that was conducted by the Electrostatics and Surface Physics Laboratory (ESPL) at the National Aeronautics and Space Administration (NASA) Kennedy Space Center (KSC). The team at ESPL conducted an electrostatic discharge hazard investigation on the telemetry antenna for the self-destruct system of an ARES-1 launch vehicle. Subsequently, the team derived a theoretical Paschen's Law model that consider the Mach number of the vehicle and the dynamic pressure. The theoretical model was then revised to consider compressibility effect experienced by the launch vehicle. The revised theoretical Paschen's Law model was used for the validation experiment in the investigation presented in this work [1, 2].

To validate the theoretical model an electrostatic discharge event must be capture during the supersonic flow. Additionally, the gap height (i.e. separation of the conductive surfaces) and discharge voltage must be known. This information was sufficient to plot the data over the theoretical Paschen's Law curve for comparison.

The supersonic facility at the Center for Advanced Turbomachinery & Energy Research (CATER) at the University of Central Florida was used to simulate the environment of a launch vehicle. The facility provided a supersonic test section at Mach numbers 1.5 to 3.75. The run time ranged

between 5 to 10 seconds depending on the set Mach number. The test section was equipped with a sting mount, which was used to hold the electrode that produced the ESD event.

The design of the electrode was particularly challenging because it required significant trade-offs between optimal geometry for supersonic flow versus optimal geometry for electrostatic charging. Several design iterations are presented in this work. The first iteration was a slender and rounded aluminum electrode. After structural testing it was found that a more robust design was needed. The major issue was excessive deflection which then lead to flutter and yielding. The next few iterations used a thicker and sharper 304 stainless steel electrode to increase the structural stability. After an FEA analysis, structural testing and aerodynamic testing it was found that the optimal electrode design was a rounded wedge-like geometry. The rounded feature satisfied the electrostatic requirements which aimed at avoiding corners which accumulate high electric field regions. The wedge-like feature satisfied the aerodynamic requirement which allowed supersonic flow to be established around the electrode with minimal blockage.

The flow features around the electrode are discussed. These features included a bow shock, Mach reflections and reflected shock waves. It was worth noting that these features would alter the flow parameters such as Mach number, static pressure, velocity and pathlines. A Z-type schlieren imaging system was used to visualize these features. This method uses a collimated beam of light to highlight density gradients in a flow [3]. This has been proved to be especially useful in supersonic flows because the shock waves cause large density gradients and are easy to visualize.

Chapter 3 discusses the experimental results with the use of plots and analysis. The effects of ESD events and plasma in supersonic flows have been studied by many scientists [4- 15]. There are

three major mechanism through which plasma interacts with supersonic flow. One of these was magnetohydrodynamic (MHD) effects which utilizes a large external magnetic force to maintain a plasma cord near the surface of a supersonic vehicle to reenergize the boundary layer and prevent flow separation [4-6]. Another mechanism is thermal dissipation. This configuration typically uses a series of plasma cords which creates a thermal wedge-like structure resulting in an induced shock wave. This mechanism has been proposed for shock control in scramjet inlets [7-11]. The third effect manifest through electrostatic interaction. These effects are used to control charge flows with other electrostatic forces [12, 13]. These three mechanisms required a plasma cord and kilowatts of power. These effects do not play a major role in the theoretical model validation experiments because it does not use plasma cords and only uses around 50 W of power. ESD events have also been studied by Ernst Mach. His work used a schlieren imaging system to capture shockwaves emanating from an ESD event [16]. This event was expected in the validation experiment because ESD event were occurring in the flow. However, it was expected to be different because the introduction of the supersonic flow will alter the behavior of the emanated shock waves. These ESD induced shockwaves were expected to have an influence on the pressure measurements. Those effects were observed and quantified Chapter 3.

The ESD events were observed during a Mach 1.7 flow. This was the highest Mach number that could be used and still induce an ESD event at 35 kV, which was the limit of the power supply. Without flow the ESD event would start at around 20 kV. Once the flow was established the ESD events started to decrease in frequency. The ESD event were observed during the transient flow conditions and during the steady supersonic flow conditions. The ESD events during the steady flow were used for the rest of the investigation.

The pressure measurements were gathered by a dynamic pressure sensor and a static pressure transducer. These measurements were taken at about 1 cm apart from each other. The ESD events are clearly notable in the pressure traces presented in Chapter 3. The variation in the pressure traces with ESD events was quantified. The static pressure sensor had the largest pressure variation and highest fluctuation.

The pressure and voltage measurement were used to plot the data points on a Pachen's Law curve. The final figure Chapter 3 illustrated the Classical Paschen's Law, the theoretical Paschen's Law model with the compressible dynamic pressure term for a Mach 1.7 flow and the data points gathered during the validation experiments. It's clear that the data demonstrated good agreement with the theoretical model. Even with the pressure fluctuations that were recorded the data still lies closer to the theoretical model than the classical Paschen's Law. Therefore, the study provides a basis for validation of the theoretical model.

It was suggested that future work includes a custom-built supersonic wind tunnel facility that has the capability of variable pressure and a downstream vacuum chamber to be able to study more pressure points along the Paschen's Law curve. Further instrumentations such as an array of pressure measurements and a PIV system would also reveal valuable insight into the physics of the ESD and supersonic flow interaction. These investigations would further validate the theoretical model.

# CHAPTER 2: THEORETICAL PASCHEN'S LAW MODELS AND VALIDATION EXPERIMENT

## 2.1    <u>Introduction</u>

Aerospace vehicles are often required to operate under extremely harsh environments. One such instance can be encountered when a rocket traverses the atmosphere at supersonic speeds. Rockets often encounter dust and ice crystals within clouds which lead to elevated levels of triboelectric charging. Triboelectric charging is a type of contact electrification through which a material becomes electrically charged after coming into frictional contact with a different material [1]. An Air Force report summarizes that a F-4D Phantom II, a supersonic aircraft, has shown that a charge with a voltage of up to 100 kV can accumulate at the surface of a vehicle. This aircraft was flying at similar conditions experienced by rockets during part of their flight envelop. This issue has concerned engineers in charge of the ARES-I rocket. Engineers asked the subject-matter-experts (SMEs) at the Electrostatics and Surface Physics Laboratory (ESPL) at NASA Kennedy Space Center (KSC) to investigate the risk of electrostatic discharges to the self-destruct systems antenna [2].

The ESPL report on risk associated with potential discharge to the antenna from triboelectrically charging demonstrated that no damage would occur during the flight envelope of the ARES-I rocket. However, the report highlighted that there was a lack of knowledge in the effects of compressible flows and high bulk flows over discharge voltage (i.e. sparking voltage). The voltage discharge is predicted by the Classical Paschen's Law. This law takes into consideration many factors related to the electromagnetic field, material properties, carrier gas properties and electrode geometries. However, it does not consider a net velocity and/or pressure change over the surface

of the conducting electrodes. This law is typically acceptable for low speed flows since there are no significant effects on the medium density. It is expected that for compressible flows the Classical Paschen's law would fail to predict the voltage discharge event due to compressibility effects (i.e. $\Delta\rho > 5\%$) and high bulk flow rates. Dr. Michael D. Hogue, from the ESPL laboratory at NASA KSC, developed several theoretical Paschen's Law models that considered Mach number, dynamic pressure and compressible pressure terms. The basic hypothesis of the theoretical models is that the number of electron-ion pairs created per unit distance between electrode surfaces are mitigated by the electron-ion pairs removed per unit distance by the high bulk gas flow rates. An apparent discharge path that is comparable to the velocity profile of the carrier gas flow was also identified [17].

The objective of this work was to validate the theoretical models using the CATER Supersonic wind tunnel capabilities to simulate the spacecraft moving through the atmosphere. The research expands on the proof-of-concept research done under the NASA Science Innovation Fund (SIF) to provide supersonic wind tunnel experimental data of the electrical discharge under supersonic conditions and validate the developed modified versions of Paschen's Law. The work also has the potential to enhance the launch criteria for triboelectric charging due to atmospheric dust or ice crystal impingement on spacecraft surfaces. If so considerable launch costs (ROM of around a million U.S. dollars) could be saved. Also, improved anti-static coatings could be developed based on the results of this work. The performance and limitations of spacecraft vehicles continues to be influenced by electrostatic interference. Electrostatic discharge by ice crystals at high-altitude supersonic-flows can lead to severe consequences affecting the safety of aerospace vehicles (i.e., 2010 ice crystal impingement on the NASA Ares I self-destruct system). Developing new models

that capture Mach number and dynamic pressure effects will facilitate electrostatic discharge attenuation [17].

## 2.2    The Classical and Modified Theoretical Paschen's Law Models

These formulations are first presented by Dr. Michael Hogue from the ESPL at NASA KSC [17]. They are recreated here to connect the objective of the work with the theoretical model.

### 2.2.1    Classical Paschen's Law

The Paschen's law [18], relates the sparking voltage (i.e. breakdown voltage) between two electrodes to ambient gas pressure, $P$, and the electrode separation gap, $d$. Once the breakdown voltage, $V_s$, is reached an electrostatic discharge occurs between the charged electrodes. Additional constant parameters within the Paschen's law are the ionization potential of the ambient gas, $V_i$, the atmospheric pressure at sea level, $P_a$, the molecular mean free path at sea level, $L$, and the secondary electron emission coefficient of the electrode material, $\gamma$. The Classical Paschen's law is illustrated in Eq. (1) [17]. As the electric potential builds up between the electrodes, it charges the small number of electron-ions typically present in the air. The particles then separate and move towards the oppositely charged electrode. Along the way, the particles can strike and ionize other atoms and molecules thus creating a cascade of charged particles (i.e. Townsend cascade effect) that eventually results in an electrostatic discharge [17].

$$V_s = \frac{\frac{V_i}{L*P_a}P*d}{ln(P*d) - ln[L*P_a*ln\left(1+\frac{1}{\gamma}\right)]} \tag{1}$$

7

The hypothesis is that the number of electron-ion pairs created per unit distance is reduced by the electron-ion pairs removed per unit distance by high bulk flow rate of gas passing over the gap between the electrodes. To consider this effect a modified equation must be a function of the mean velocity, $v_{xm}$, of the carrier gas. As part of the verification process the modified model must reduce to Classical Paschen's law when $v_{xm} = 0$ [17].

### 2.2.2   Mach Number Formulation

Neutral gas atoms and molecules can be come ionized by collisions with the ions that are typically in the air when an electrical potential is set between two electrodes. These electron-ion pairs separate, the electrons travel toward the positively charged electrode and the positively charged ions move toward the negatively charged electrode. If the velocity of these charged particles is great enough (kinetic energy of $E \geq V_i$), then other atoms and molecules become ionized. These newly formed electron-ion pairs will separate and collide with other neutral particles creating what a cascade of charged particles leaving the mediating gas between the electrodes more conductive than before. This forms a repetitive process that eventually leads to an electrostatic discharge (i.e. sparking) between the electrodes. The number of new electron-ion pairs, $dn$, can be calculated using the Eq. 2 [17].

$$dn = n * \alpha * dx \tag{2}$$

The ionization coefficient, $\alpha$, can be defined as the number of electron-ion pairs created per unit distance. For moving gas, some coefficients that deal with the removal and addition of electron-ion pairs from the perimeter of the electrodes must be defined. The term $\beta$ was defined as the

electron-ion pairs per unit distance lost and $\hat{\delta}$ as the electron-ion pairs per unit distance added from the introduction of the gas flow [17]. This altered the form of Eq. (2) to the following

$$dn = n * (\alpha - \beta + \delta) * dx = n * \alpha' * dx \qquad (3)$$

Unless the ambient gas is fairly ionized to begin with, the effect of the δ term can be neglected so that Eq. (3) can be simplified to the form of

$$dn \cong n * (\alpha - \beta) * dn \cong n * \alpha' * dx \qquad (4)$$

Separating variables, then integrating over the separation of the electrodes $(0 - d)$, and solving for the number of electrons, $n_e$,

$$\int_0^{n_e} \frac{dn}{n} = \alpha' * \int_0^d dx \qquad (5)$$

$$n_e = e^{\alpha' * d} \qquad (6)$$

To get the number of ions, $n_i$, we must subtract one from the number of electron, then

$$n_i = e^{\alpha' * d} - 1 \qquad (7)$$

When positive ions strike the cathode, electrons are released and travel to the anode. The probability per ion that electrons are released from this event is called the secondary electron emission coefficient of the conductor, γ. The self-renewing breakdown condition is the Townsend's regeneration condition [17].

$$\gamma * (e * \alpha' * d - 1) = 1 \qquad (8)$$

If we solve solving Eq. (7) for $\alpha'$ we get the following form

$$\alpha' = 1 * d * \ln(1 * \gamma + 1) \qquad (9)$$

There are two fundamental assumptions needed to derive the Paschen's law.

1.      Each electron, moving a distance $(0 \leq l \leq d)$ through an electric field, $E$ between the electrodes gap, loses all its kinetic energy, $KE$ upon impact with other particles.

2.      Each electron can ionize a neutral particle when its kinetic energy, $q_e*E*l$, (where $q_e$ is the charge on the electron, 1.602 x 10$^{-19}$ Coulomb) was equal to the ionization potential, $V_i$, of the carrier gas.

To get an energy $q_e*V_i$, an electron must move a distance $y_i$. The probability of this is given by [19]

$$e^{\frac{-y_i}{l}} = e^{\frac{-V_i}{E*l}}$$  ( 10)

where $1/l$ is the number of impacts per unit distance.

The hypothesis is that the ambient gas flow causes a loss of electron-ion pairs around the electrodes and the probability of this is given by a dimensionless aerodynamic term that is proportional to the ambient gas velocity, $v_{xm}$. The aerodynamic function that was used for this derivation was the Mach number, $M_N = v_{xm}/c$ where $v_{xm}$ is the mean gas velocity and $c$ is the speed of sound [20]. Equation 9 can be used to calculate the number of electron-ion pairs added per unit distance and those removed by the gas flow with the addition of a Mach number term for this formulation.

$$\alpha' = \frac{1}{l} * e^{-\frac{V_i}{E*l} - M_N}$$  ( 11)

Let the electric field at discharge be $E = V_s/d$ and substituting into Eq. (10) we get

$$\alpha' = \frac{1}{l} * e^{-\frac{V_i*d}{V_s*l} - M_N}$$  ( 12)

Using $l = L*P_a/P$ and setting Eqns. (8) and (11) equal and solving for the discharge voltage we can get the new formulation in terms of pressure and the aerodynamic parameter

$$V_S = \frac{\frac{V_i}{L*P_{atm}}*(P*d)}{\ln(P*d)-\ln\left[L*P_{atm}*\ln\left(1+\frac{1}{\gamma}\right)\right]-M_N} \qquad (13)$$

Eq. (13) is a form of the Classical Paschen's law, Eq. (1), with simply the Mach number term in the denominator. By setting $v_{xm} = 0$, it can be shown that this equation reverts to the Classical Paschen's law. Equation (13) and the Classic Paschen's Law are shown in Fig. 2-1.

It can be seen in Fig. 2-1, that the addition of the Mach number to modify the number of electron-ion pairs formed between the electrodes results in an increase in discharge voltage. It was worthy to note that this effect was more dominant at lower P*d values [17].
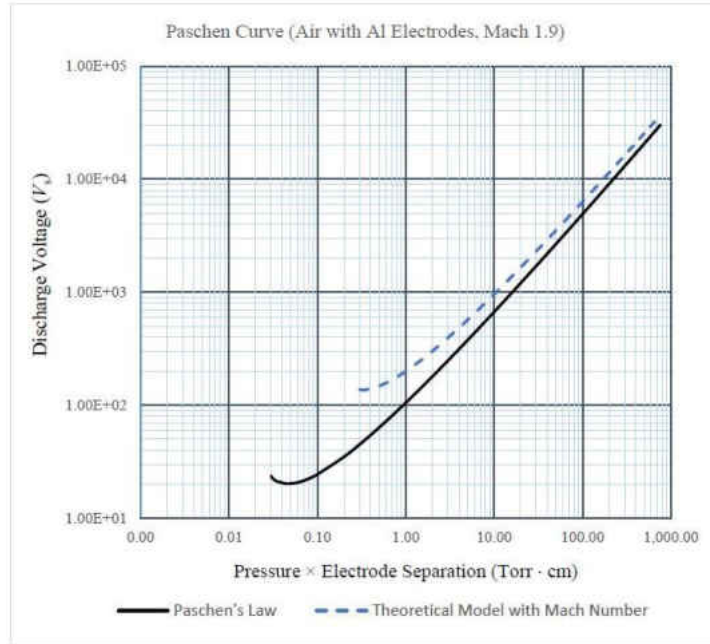
**Figure 2-1: Theoretical Paschen's Law with Mach number term**

Source: Hogue, Michael, D., Kapat, Jayanta, Ahmed, Kareem, Cox, Rachel, E., Wilson, Jennifer, G., Calle, Luz, M., and Mulligan, Jaysen. "Dynamic Gas Flow Effects on the ESD of Aerospace Vehicle Surfaces" Proc. 2016 Electrostatic Joint Conference, Purdue Univeristy, June 13-16, 2016.

### 2.2.3   Mach Number and Dynamic Pressure Term Formulation

In fluid mechanics, the total pressure term, $P_0$, is an addition of the static and dynamic pressure term, $P_D$. For $v_{xm} = 0$, the total pressure term is equal to the dynamic pressure term. However, for $v_{xm} >> 0$ the dynamic pressure term is much more significant. The dynamic pressure term can be expressed in terms of mean gas velocity as

$$P_D = \frac{1}{2} * \rho * v_{xm}^2 \qquad\qquad (14)$$

12

where $\rho$ is the carrier gas density. Then the total pressure term becomes

$$P_0 = P_s + P_D = P_s + \frac{1}{2} * \rho * V_{xm}^2 \qquad (15)$$

Assuming ideal gas law we can relate

$$P_S * \forall = \left(\frac{W}{M}\right) * R * T \qquad (16)$$

where $\forall$ is specific volume, $M$ is the molecular weight of the carrier gas, $W$ equals the number of moles times the molecular weight, $R$ is the universal gas constant, and $T$ is the temperature of the carrier gas.

$$\frac{P_S * M}{R * T} = \left(\frac{W}{M}\right) * R * T \qquad (17)$$

This equation can be re-written in terms of Mach number as follows

$$P_0 = P_S + \frac{1}{2} * \left(\frac{P_S * M_N}{R * T}\right) * v_{xm}^2 = P_S * \left(1 + \frac{1}{2} * \frac{M_N}{R * T} * v_{xm}^2\right) \qquad (18)$$

Assuming the compressibility factor, $Z \sim 1$ and substituting Eq. 18 into Eq. 13 we get the following form of the Paschen's Law that considers Mach number and an incompressible dynamic pressure term

$$V_S = \frac{\frac{V_i}{L * P_a} * \left(1 + \frac{1}{2} * \frac{M_N}{R * T} * v_{xm}^2\right) * P_S * d}{\ln\left[\left(1 + \frac{1}{2} * \frac{M_N}{R * T} * v_{xm}^2\right) * P_S * d\right] - \ln\left[L * P_a * \ln\left(\frac{1}{\gamma} + 1\right)\right] - M_N} \qquad (19)$$

Equation 19 was plotted next along with the Classical Paschen's law in Fig. 2-2. This relation resulted in an even higher discharge voltage for the same $P*d$ term. When $v_{xm} = 0$, Eq. 19 reverts to the Classical Paschen's law [17].



Paschen Curve $M_N$ & Dynamic Pressure (Air with Al Electrodes, Mach 1.9)
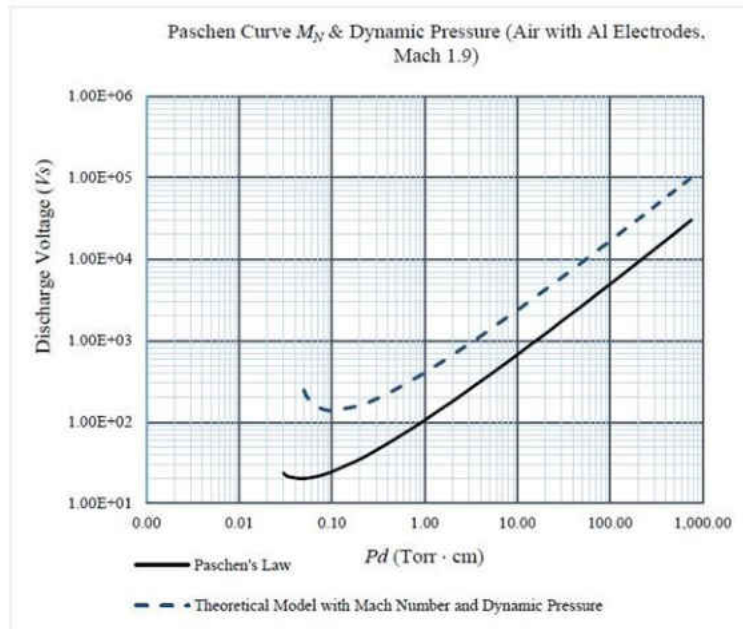
Fig. 2. Paschen's Law compared to the revised Mach number formulation with dynamic pressure terms.

**Figure 2-2: Theoretical Paschen's Law with Mach number and Incompressible Dynamic**

**Pressure Term**

Source: Hogue, Michael, D., Kapat, Jayanta, Ahmed, Kareem, Cox, Rachel, E., Wilson, Jennifer, G., Calle, Luz, M., and Mulligan, Jaysen. "Dynamic Gas Flow Effects on the ESD of Aerospace Vehicle Surfaces" Proc. 2016 Electrostatic Joint Conference, Purdue Univeristy, June 13-16, 2016.

### 2.2.4 Mach Number and Compressible Dynamic Pressure Term Formulation

The total gas pressure is comprised by two components. One component is the static gas pressure, $P_s$, and the other one is the dynamic pressure, $P_{DI}$.

$$P_0 = P_S + P_{DI} \tag{20}$$

Because we are considering compressible flow (i.e. Mach number greater than 0.3) we cannot use the incompressible dynamic pressure.

$$P_{DI} = \frac{1}{2} * \rho * v_{xm}^2 \tag{21}$$

Where $\rho$ is the gas density and vxm is the mean gas velocity.

Instead of simply using this the incompressible form of the dynamic pressure term we must use the compressible dynamic pressure which is derived in [21, 22]

$$P_{DC} = P_{DI} * \left[ \left( 1 + \frac{\gamma_a - 1}{2} * M_N^2 \right)^{\frac{\gamma_a}{(\gamma_a - 1)}} - 1 \right] * \frac{2}{\gamma_a * M_N^2} \tag{22}$$

Where $\gamma_a$ is the ratio of specific heats for the ambient gas (for air at STP conditions, $\gamma_a = C_P/C_V = 1.4$). The incorporated incompressible dynamic pressure, $P_{DI}$, from Eq. (3), can be written in terms of $\gamma_a$ and $M_N$ like so

$$P_{DI} = \frac{1}{2} * \rho * v_{xm}^2 = \frac{1}{2} * \gamma_a * M_N^2 * P_S \tag{23}$$

Substituting Eq. (6) into Eq. (5) we get

$$P_{DC} = P_S * \left[ \left( 1 + \frac{\gamma_a - 1}{2} * M_N^2 \right)^{\frac{\gamma_a}{\gamma_a - 1}} - 1 \right] \tag{24}$$

Substituting Eq. (7) into Eq. (2) we get the discharge voltage in an air gap at STP conditions (with $P_0 = P_s + P_{DC}$). This is a new formulation of the Paschen's law that considered both and aerodynamic parameter and compressibility effects

$$V_s = \frac{\frac{V_i}{L*P_a}*\left(1+\frac{\gamma a-1}{2}*M_N^2\right)^{\frac{\gamma a}{\gamma a-1}}*P_S*d}{\ln\left[\left(1+\frac{\gamma a-1}{2}*M_N^2\right)^{\frac{\gamma a}{\gamma a-1}}*P_S*d\right]-\ln\left[L*P_a*ln\left(\frac{1}{\gamma}+1\right)\right]-M_N} \qquad (25)$$

Letting $v_{xm} = 0$, Eq. (8) reverts to classical Paschen's law. This formulation is plotted in Fig. 2-3 for stainless steel (SS) electrodes ($\gamma = 0.02$, [17]) at several Mach numbers for air ($\gamma a = 1.4$) between 0.5 and 3.75 and an electrode separation (i.e. gap) of 1.3 cm [17].
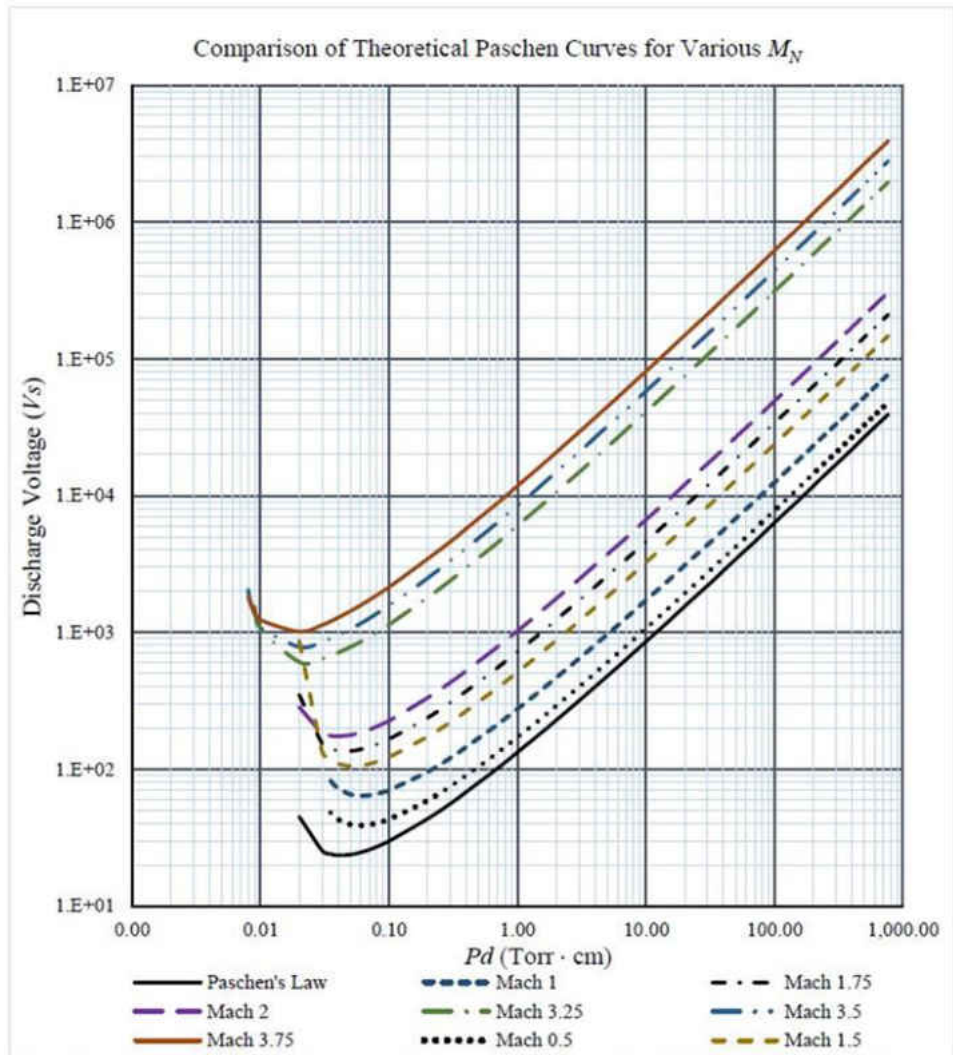
**Figure 2-3: Theoretical Paschen's Law with Compressible Dynamic Pressure Term**

Source: Hogue, Michael, D., Cox, Rachel, E, Mulligan, Jaysen, Kapat, Jayanta, Ahmed, Kareem,

Cox, Rachel, E., Wilson, Jennifer, G., and Calle, Luz, M. "Revision of Paschen's Law Relating

to the ESD of Aerospace Vehicle Surfaces" *Proc. 2017 Electrostatic Joint Conference,*

*University of Ottawa, June 13-15, 2017*.

### 2.2.5 Apparent Effective Discharge Path

A velocity profile can be seen by taking a cross-section of a channel with flow [17]. The velocity profile is typically parabolic for laminar flows and top hat in shape for turbulent flow with zero velocity (i.e. no slip) condition at the channel walls and is maximum at the channel center. Figure 2-4, shows velocity profile data from a Mach 1.47 wind tunnel experiment [17].
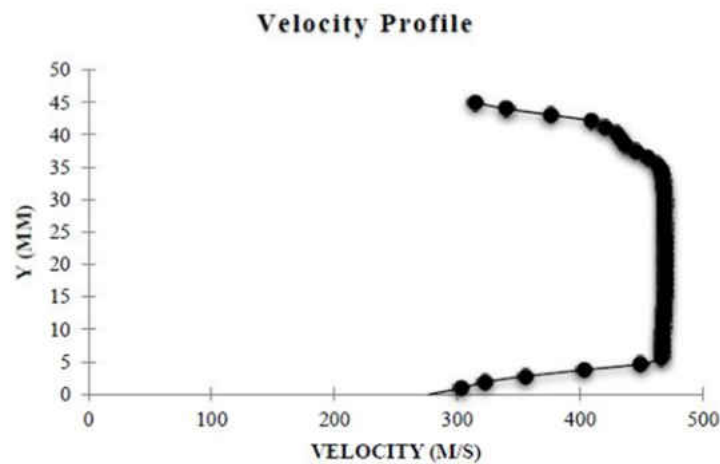


**Figure 2-4: Velocity Profile at Mach 1.47**

Source: Hogue, Michael, D., Cox, Rachel, E, Mulligan, Jaysen, Kapat, Jayanta, Ahmed, Kareem, Cox, Rachel, E., Wilson, Jennifer, G., and Calle, Luz, M. "Revision of Paschen's Law Relating to the ESD of Aerospace Vehicle Surfaces" *Proc. 2017 Electrostatic Joint Conference, University of Ottawa, June 13-15, 2017.*

When air flows in a channel, a velocity profile is created [21, 22]. This velocity profile is typically parabolic in shape with zero velocity at the channel walls and is maximum at the channel center.

This velocity profile is linear across the center of the 4.4 cm wide channel because the length of the test section did not allow for the typical parabolic shape to develop [21, 23].

At a one to one scale, the perimeter around the velocity profile in Fig. 2-4 measured 11.7 cm. From inspection of Eq. (25) we hypothesize an expression for an effective electrode separation.

$$d' = \left(1 + \frac{\gamma_a - 1}{2} * M_N^2\right)^{\frac{\gamma_a}{\gamma_a - 1}} * d \qquad (26)$$

For air ($\gamma a = 1.4$) at Mach 1.47 and d = 4.4 cm, we get for Eq. (9)

$$d' = \left(1 + 0.2 * M_N^2\right)^{3.5} * d = 15.48 \, cm \qquad (27)$$

This gives a value around 25% larger than the 11.7 cm distance graphically measured along the flow profile in Fig. 2-4. Analysis of other wind tunnel velocity profile data with different channel widths and Mach numbers will be necessary to better evaluate this hypothesis [17].

## 2.3    Development of Validation Experiment

### 2.3.1   Objective of Proposed Experiment

The objective of the proposed experiment was to provide proof-of-concept for the theoretical models. To do so the electrodes must experience a supersonic flow within a constant gap. The gap width, static pressure measurements and Mach number are needed to plot the data in a Paschen's law graph.  The goal of this work is to provide a proof-of-concept and order magnitude of the effects of supersonic flow on the discharge voltage.

### 2.3.2 Constraints of Experimental Development

The highest voltage that could be provided by the high voltage power supply (HVPS) available was 60kV however the insulated teflon wire used for the experiment can only reach 40kV. Therefore, a safe operating limit was set at 35kV. Another general constrain was the air reservoir which was the building medium pressure air reservoir outside of the CATER facility. The air reservoir was 18.9 $m^3$ in volume and reached a maximum pressure of 18.6 bar, which resulted in a run time of 5-10 seconds depending on the Mach number. Finally, the static pressure in the tunnel was not controllable because the facility operated as a blowdown facility, meaning that the value did not regulate the flow pressure upstream of the test section.

### 2.3.3 Supersonic Flow Requirements

The flow in the tunnel must remain supersonic over the surface of the electrodes. To achieve this the electrodes blockage must be minimized as much as possible. The test was to be conducted at various Mach numbers ranging from 1.5 to 3.5. The static pressure must remain below atmospheric pressure during the test.

### 2.3.4 Electrostatic Parameter Requirements

The electrostatic discharge must occur between the two electrodes and be as perpendicular as possible. Discharges from the positive electrode to any other surface must be avoided to consider the test successful. To achieve this the electrodes shape must promote a uniform electric field and avoid localized high electric field spots. This requires smooth transitions, large radii and a smooth surface finish.

### 2.3.5    Structural Requirements

In addition to the supersonic flow requirements and the electrostatic requirements the electrodes must withstand the structural loads from the aerodynamic forces. The aerodynamic forces at supersonic speed become very large therefore the electrode material and geometry was influenced by this requirement.

### 2.4       Electrode Design Process

### 2.4.1    Custom Facility Design

Although the custom facility design was canceled due to funding issues it is worthy to note the design efforts to consider for follow up research efforts. The first approach at design the test facility for the experiment was building a custom facility. This would allow for good control of the facility upstream pressure which would allow us to vary the pressure in the test section. It would also allow for flush mounted electrodes which would have no blockage effects and/or shock structures in the test section. Therefore, this was the first proposed facility and the design is considered in this section. The greatest restriction of the custom facility was that it would have to be design for one Mach number, because the variable nozzle adds tremendous complexity and cost. However, various interchangeable nozzle can be design for different Mach numbers. Based on the predicted discharge voltage of 35kV, it was determined that Mach 2 would be a good set number for the first design.

2.4.1.1 <u>Converging-Diverging Nozzle Design</u>

2.4.1.1.1        Converging Section Design

The nozzle inlet was design using a 5th order polynomial method derived in a NASA Technical report. The nozzle length to height ratio, $L/H_i$, is kept between 0.89 to 1.89 to minimize the probability of flow separation in the converging section of the nozzle. If the facility is design bellow this ratio it would be prone to flow separation at the inlet due to high adverse pressure gradients. If the facility is design above this range it would then become prone to pressure separation at the exit of the converging section due boundary layer build up. The contraction ratio between 6 and 10 found to be adequate for the converging section design [24].

The converging nozzle that was design for this facility had an $L/H_i$ ratio of 1.34 and a contraction ratio of 8. These ratios were about half way between the upper and lower limits. The nozzle inlet height was around 16 cm and while the exit was 2 cm. Figures 2-5 & 2-6, show the normalized and actual nozzle contour plots, respectively.
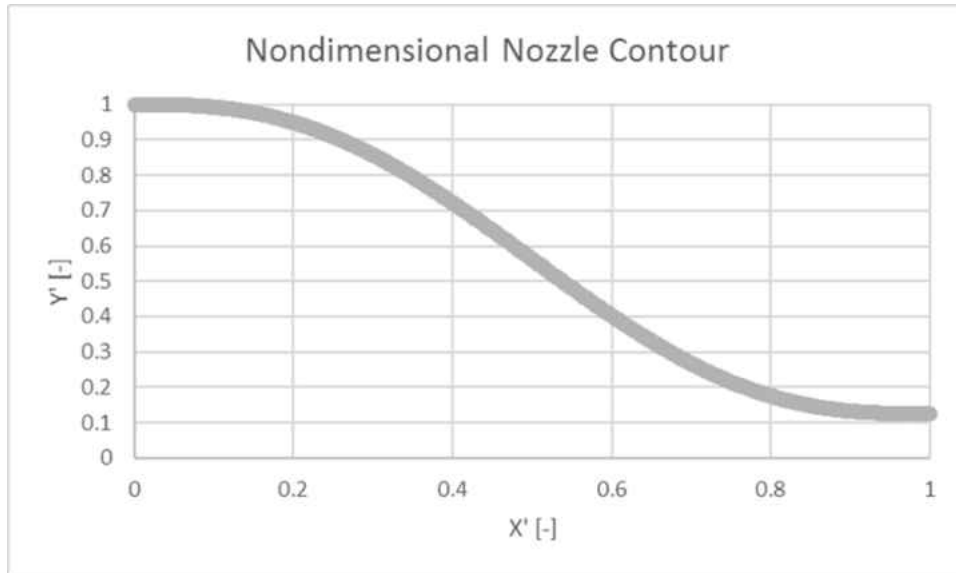
**Figure 2-5:  Normalized Converging Nozzle Contour Design with 5th Order Polynomial**
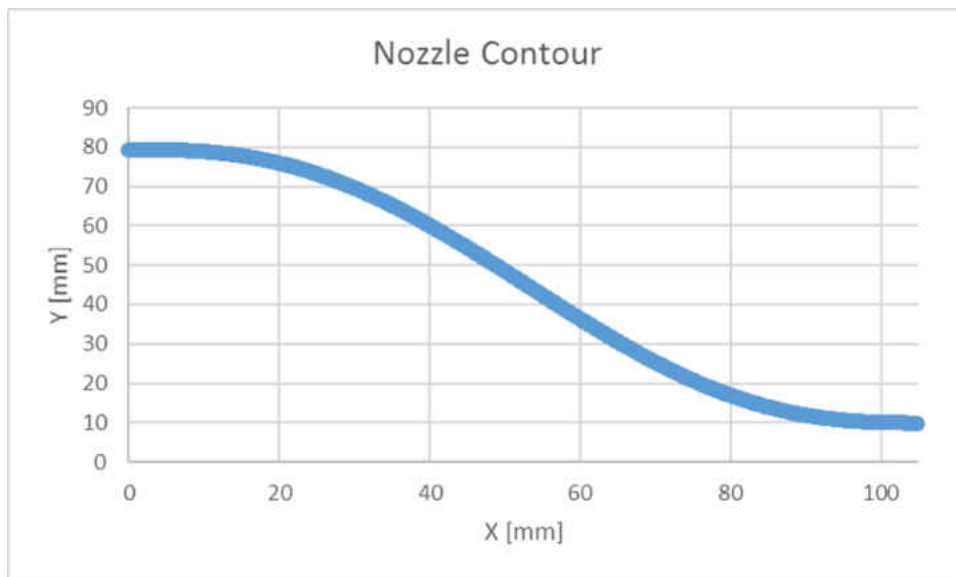


**Figure 2-6: Converging Nozzle Contour Design with 5th Order Polynomial**

2.4.1.1.2        Diverging Section Design

The method of characteristics can be used to develop a contour for the design of the diverging based on expanding the flow through this portion of the nozzle without coalescing Mach waves into a shock wave. It is best to develop an algorithm to carry out these calculations and plot the contour [20].

2.4.1.2 Test Section

A maximum height of two cm between the test section bottom and top wall was part of the initial design requirements. This was because the electrodes were required to be flush mounted and the maximum "gap" between the electrode was required to be two cm. This was determined based on the high voltage power supply (HVPS) limitation and the geometry of the electrodes. These calculations are from the Paschen's law equation. The length and width of the test section did not have strict requirements; however they were required to be at a distance of at least twice that of the gap between the bottom and the top wall from the electrodes. Another restriction on the length of the tunnel test section was the friction from the walls. Calculations showed that because the tunnel height was so small the Fanno flow quickly degraded the supersonic flow to the chocking point, therefore a shorter test section was desired. A Mach number versus test section length is shown in Fig. 2-7. The parameters for these calculations were surface friction coefficient, $f$, channel length, $L$, and the hydraulic diameter of the test section, $D_h$. The surface friction coefficient was set to 0.004. This was calculated from based on the surface of the material chosen for the test section which was Delrin©.  The length of the channel was set to a range of 0 cm to 32 cm and the

hydraulic diameter was calculated to be 1.74 cm. This resulted in a f*D/L value of 0.305 for

chocked flow.
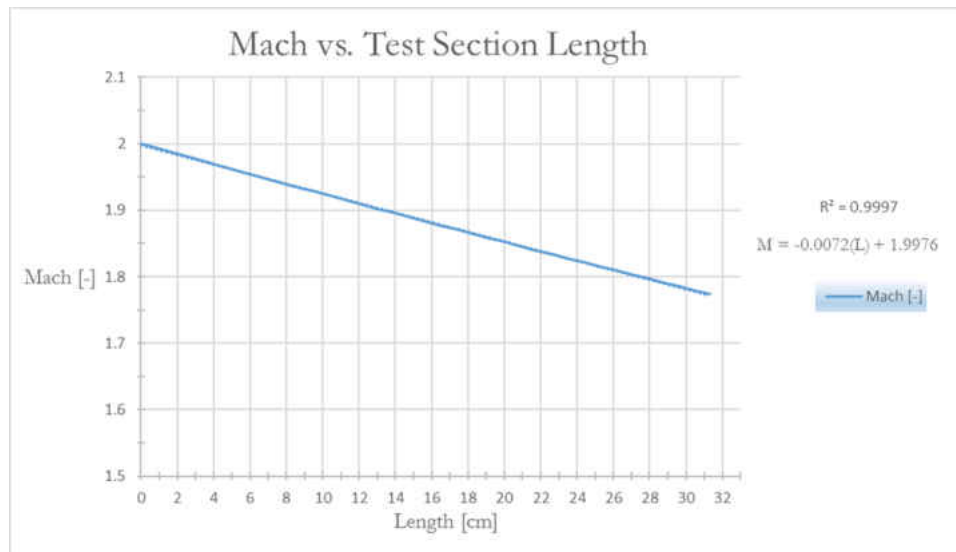


**Figure 2-7: Fanno Loss and Mach Number Along Test Section**

A test section length of about 17 cm was selected. This allowed for a 10-cm electrode to have a

clearance upstream from the nozzle of 5 cm and downstream from the exit of 2 cm. The Mach

number over the electrode varied from 2 to 1.9 due to the pressure losses associated with Fanno

flow. This was illustrated in Fig. 2-8.
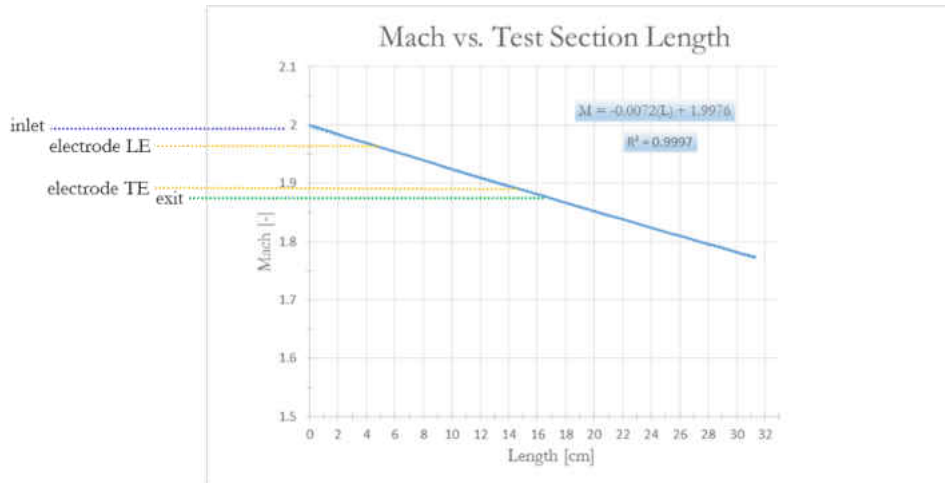
**Figure 2-8: Electrode Placement in Test Section**

Another necessary requirement was that the electrodes are completely insulated from the tunnel walls. A required distance of at least two times the electrode width between the electrode and any other conductive material was set as part of the precautions to avoid unintended electrostatic discharges. As seen in Fig. 2-9, a "sandwich" method was used to incase the electrodes in a Delrin © sleeve which provided a high dielectric material that has a large modulus of elasticity for mechanical strength and a working temperature below the minimum expected temperature for the Mach 2 flow. The expected temperature for the Mach 2 flow was 165 K.
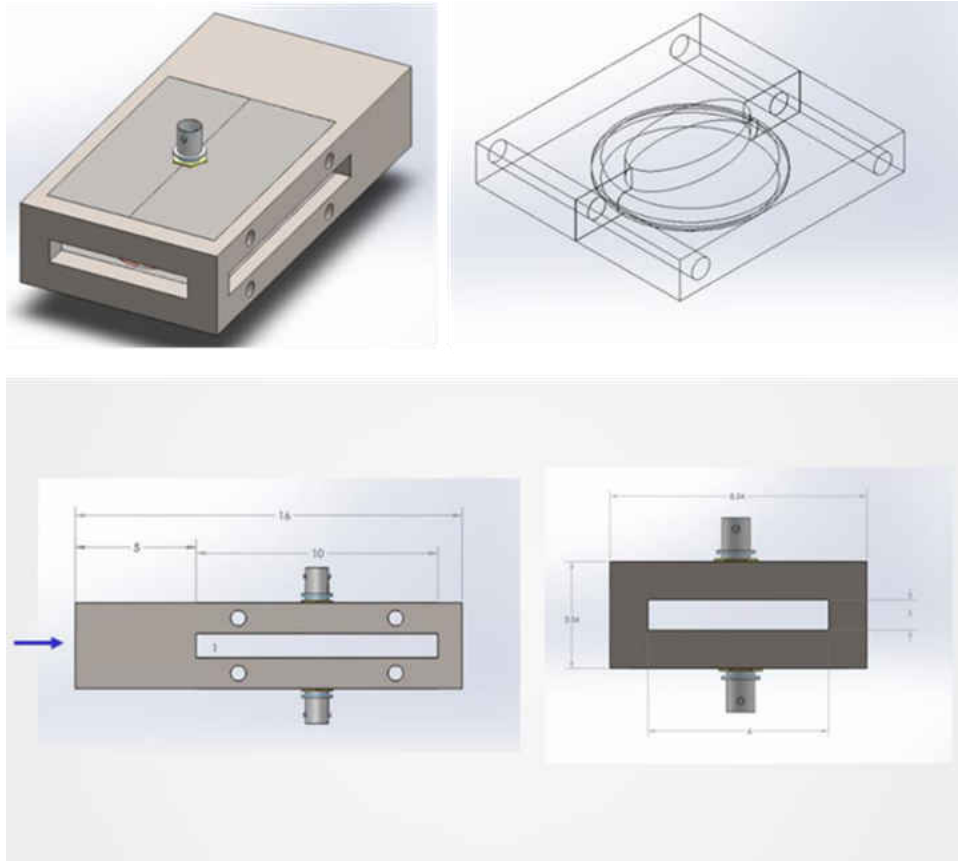
**Figure 2-9: Test Section CAD with Electrode Mounts**

2.4.1.3 Operating Parameters

The supersonic facility would be operated with a regulator upstream which would be set at the minimum pressure needed to run the Mach 2 flow with a Fanno flow in the test section and a normal shock standing at the exit.

2.4.1.4 Custom Supersonic Facility Design

Figure 2-10, illustrate the design of the custom supersonic wind tunnel facility. The settling chamber attached to the large diameter pipe extending from the building air reservoir. This was a

dump type settling chamber which allows the flow to expand and straighten before entering the converging section of the C-D nozzle.
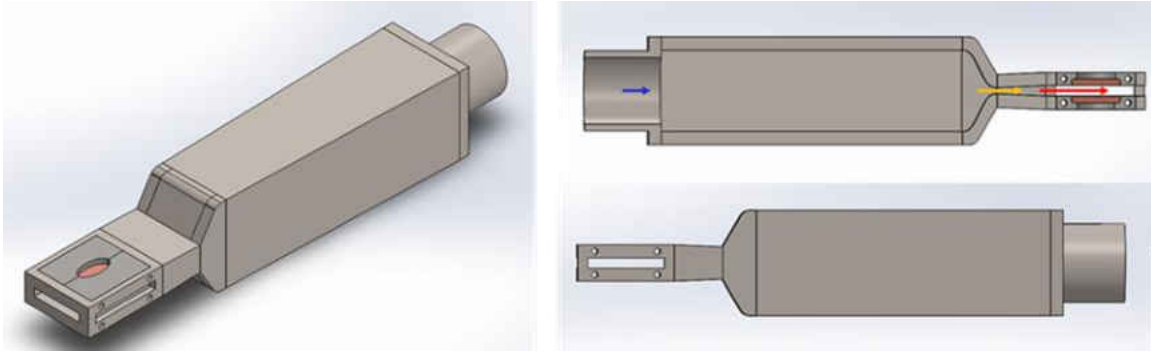


**Figure 2-10: CAD of Custom Facility**

### 2.4.2 Supersonic Blowdown Facility (SBF) Sting Mount Design Process

Due to funding constraints with this phase-one project the custom design facility was not pursued. However, this facility design could be used for the phase-two project proposal. It will provide more control and broader data capabilities. In addition, if viewing windows are added to the facility it will provide particle image velocimetry (PIV) capabilities.

This section will focus on facility that was used for the experimentation. This facility was the second option available to run the experiment within the budgetary constraints of the project.

**Figure 2-11: Supersonic Blowdown Facility**

2.4.2.1 Facility Operating Conditions

Figure 2-11, shows the existing CATER supersonic blowdown facility which was utilized for this

investigation. This facility is supplied by the same dry air supply reservoir mention in the previous

section. Table 2-1, provides the facility parameters.

**Table 2-1: Supersonic Blowdown Tunnel Parameters**

| Mach number | 1.5-3.75 | - |
|---|---|---|
| Reynolds number | 2.9 x 106 -5.5 x107 | - |
| Enthalpy | $\sim$300 | kJ/kg |
| P_0_max | 240 | Psi |
| Test Section CSA | 10.2 cm x 10.2 cm | cm2 |
| Run time | 10-May | sec |
| Sting mount height | 1.3-8.8 | cm |
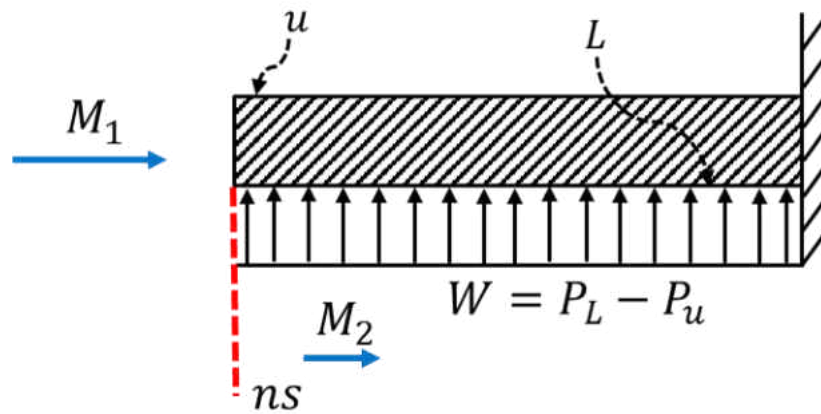
**Figure 2-12: Aerodynamic Load Assuming Normal Shock at Leading Edge and Cantilever
Beam**

Figure 2-12, shows a scenario that would result in the highest relative aerodynamic bending load
on the electrode would be if one of the surfaces experience subsonic flow and while the other
surface experienced supersonic flow. This would create the largest static pressure difference
between the top and bottom surface of the electrode. We can derive a pressure the pressure
difference, *W* and used this to set the aerodynamic load in the FEA models.

First assume that specific heats, $\gamma = 1.4$, the gas constant for air, $R = 287 \frac{kJ}{kgK}$, that the freestream
Mach number, $M_1 = 3.2$, and the stagnation pressure, $P_{01}$ is equal to the highest chamber pressure,
*1.66 x 10³ kPa*. This results in the highest aerodynamic forces in the test section and would result
in a higher safety factor for the design

The static pressure in the free stream can be calculated from the given information and the one-
dimensional flow isentropic equations for compressible flow as follows [20]

30

$$P_1 = \frac{P_{01}}{\left(1+\frac{\gamma-1}{2}*M_1^2\right)^{\frac{\gamma}{\gamma-1}}} \qquad (28)$$

The stagnation pressure, $P_{02}$, and the Mach number, $M_2$ can be determined by using the normal shock relations [20]

$$P_{02} = P_{01} * \left[\frac{(\gamma+1)*M_1^2}{(\gamma-1)*M_1^2+2}\right]^{\frac{\gamma}{\gamma-1}} * \left[\frac{(\gamma+1)}{2*\gamma*M_1^2-(\gamma-1)}\right]^{\frac{1}{\gamma-1}} \qquad (29)$$

$$M_2 = \frac{(\gamma-1)*M_1^2+2}{2*\gamma*M_1^2-(\gamma-1)} \qquad (30)$$

$P_2$ can be calculated using one dimensional isentropic compressible flow equations at station 2 [20]

$$P_2 = \frac{P_{02}}{\left(1+\frac{\gamma-1}{2}*M_2^2\right)^{\frac{\gamma}{\gamma-1}}} \qquad (31)$$

To calculate the aerodynamic load, *W*, use the following

$$W = P_L - P_u = P_2 - P_1 \qquad (32)$$

 For this scenario where *M₁ =3.2* and *P₀₁* was set to *1.66 x 10³ kPa, W = 57.4 psi.*

This model is not linear because as the maximum aerodynamic load between *Mach 1* and *Mach 4* is reached at *Mach 1.75*, where the aerodynamic load becomes *135 psi*. This was illustrated in the Fig 2-13 bellow. This was meant to produce a model with a significant safety factor. In reality, the

stagnation pressure in the reservoir would decrease over time and the aerodynamic loads would also decrease over time.
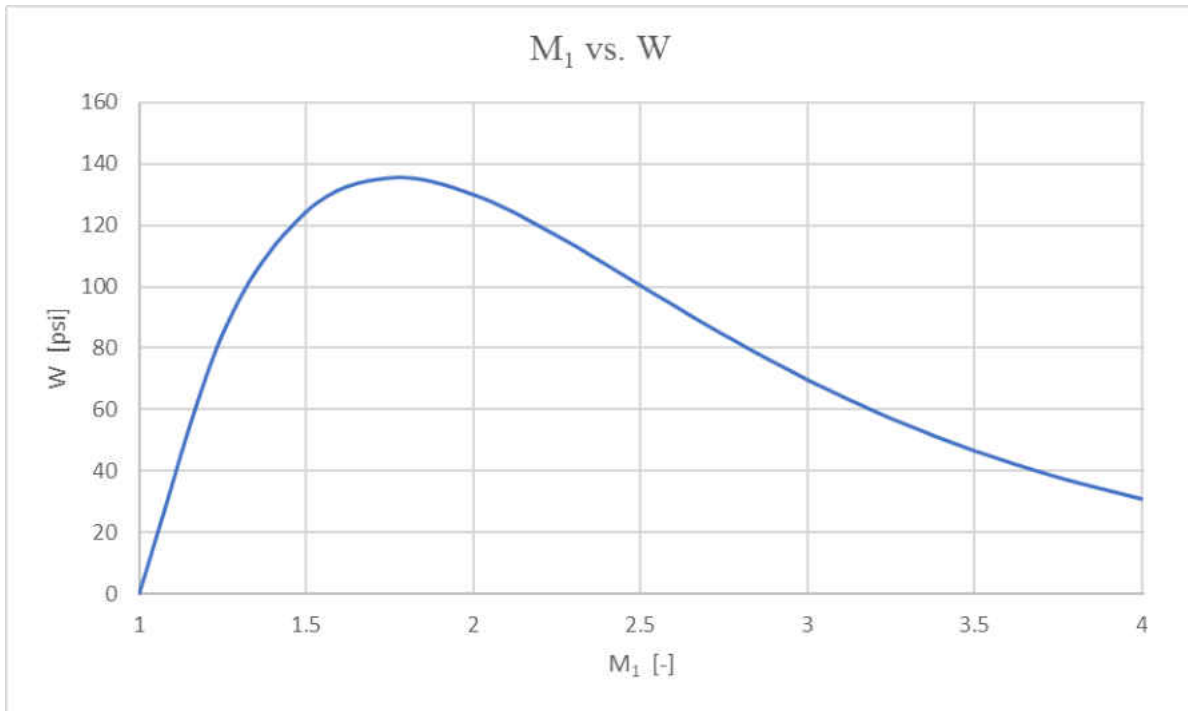


**Figure 2-13: Freestream Mach number $M_1$ versus Aerodynamic Load, W assuming a constant stagnation pressure upstream of $P_{01} = 240$ psi.**

2.4.2.2 Dual-Electrode Design

The CATER SBF has one sting mount in the test section. The initial integrated design used the sting mount to hold two electrodes in the supersonic flow. One electrode was to be the "hot" electrode or positively charged electrode and the other one was the ground electrode or negatively electrode. They are both insulated from the SBF and each other. To achieve this a PTFE sleeve was design, as shown in Fig. 2-14. Additionally, because of concern with the amount of blockage induced by the two electrodes the PTFE sleeves were made more aerodynamic by making the

leading-edges sharp. The calculated blockage (i.e. frontal area) was approximately 15% of the test section area.
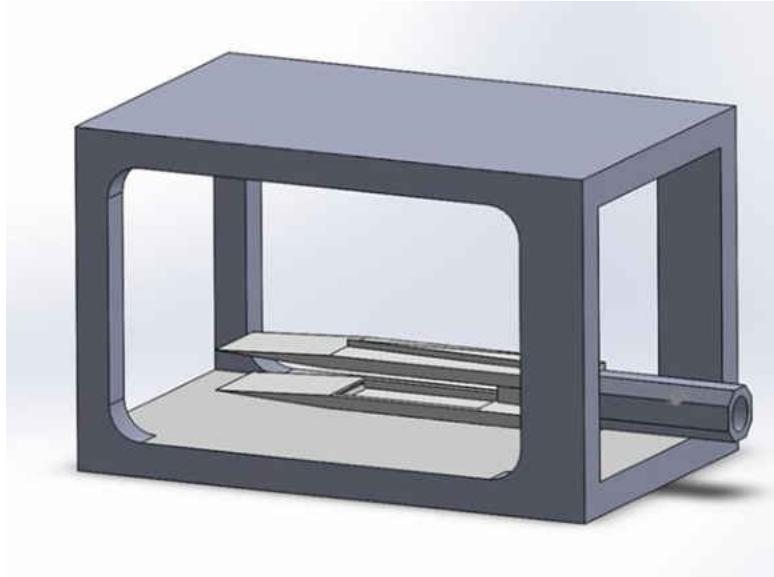


**Figure 2-14: CAD of Dual-Electrode Design in the Test Section**

A preliminary FEA, shown in Fig. 2-15, demonstrated that a PTFE sleeve would be too weak to withstand aerodynamic loads from the supersonic flow. In addition, the design was determined to be highly prone to severe shock interactions within the gap of the electrodes and a quick transition from supersonic flow to subsonic flow via an oblique shock train. Finally, this design required two electrodes, and two electrode fittings to be manufactured which increased the project cost. These three elements made the design undesirable. Another solution was proposed in the section bellow.
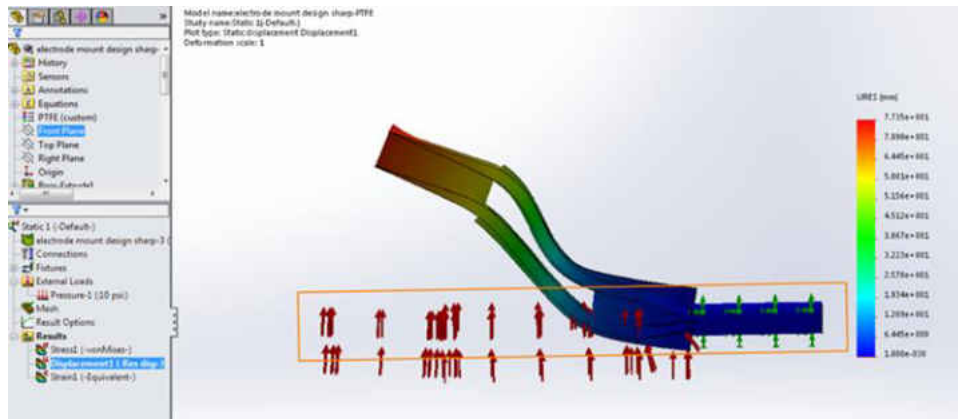
**Figure 2-15: FEA of Dual-Electrode Design at a Load of 5 psi**

2.4.2.3 Single-Electrode Designs

The single-electrode design reduced the blockage amount by more than half. As a result, the design also experiences smaller aerodynamic forces. The first iteration of the single electrode design used one electrode in the free-stream and one electrode flush mounted to the wall. The electrode on the wall acted as the ground electrode. This design required a dielectric material to insulate the ground electrode from the wall, such as Kapton or PTFE tapes. Figure 2-16, illustrated how the Kapton and PTFE tapes were applied to the bottom surface of the facility. The 2-inch-wide Kapton take has applied to over the ½-inch-wide PTFE tape because it provided a more uniform surface. As shown in Fig. 2-16, this insulation was lifted by the supersonic flow after one test.

Another attempt to insulating the bottom wall from the electrode was to cover the surface of the tapes with an epoxy. The ground electrode was a 31-mil thick sheet of 304 stainless steel. This was grounded straight to the HVPS. The ground electrode and the epoxy were sheared off the surface of the tunnel and blown out of the facility through the exhaust. The 304 SS sheet and part of the insulative tape was lost after one run of the tunnel.

34

A solution to this issue was to simply make the wall of the tunnel our ground plate, as illustrated in the bottom right of Fig 2-16. This was possible because the HVPS utilized a very small current (maximum of 1.5 mA). The facility provided enough ground for this amount of power and safe operation. For additional safety, the facility was grounded to the common ground in the CATER building, which has an Earth ground for lighting mitigation. This set up was determined to be the least complicated and most repeatable experiment. The next step was to design, fabricate and test the single electrode that was to act as the "hot" electrode.
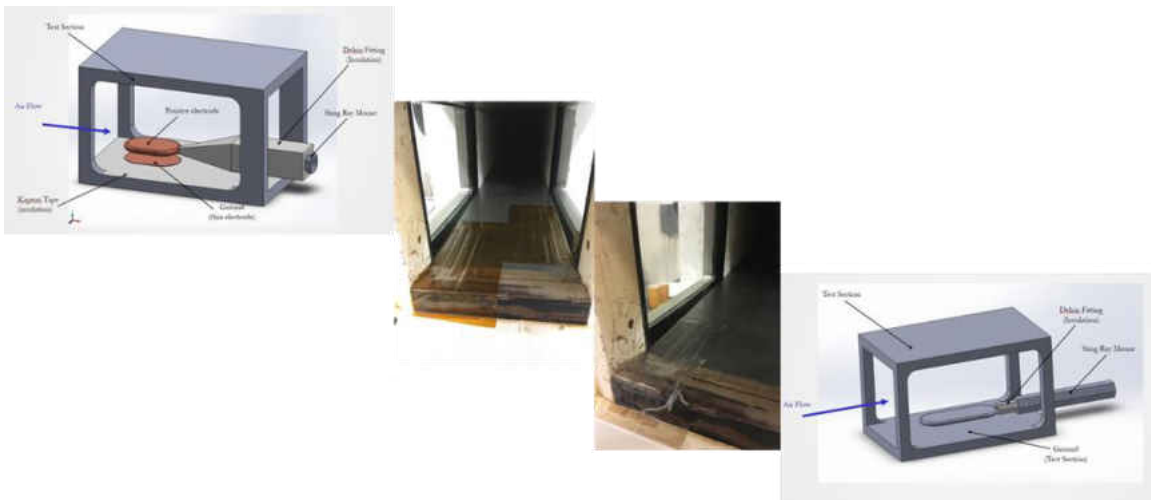


**Figure 2-16: Design Process from Dual to Single-Electrode**

2.4.2.4 <u>Hot Electrode Designs</u>

The initial design for the single-electrode was a thin rounded plate, illustrated on the right-hand side of Fig. 2-17. This electrode design was meant to be used in the custom design facility mentioned earlier. The next iteration of this design in which an extruding rod is added to the back end of the electrode, was shown on the left-hand side of Fig. 2-17. This rod would be inserted in a PTFE sleeve which then would be inserted in a cooper sleeve for structural strength. The assembly

was pressure fitted and then inserted into the facility sting mount and fasted with a set screw. The

test electrode of this test was shown in the left-hand side of Fig 2-18.
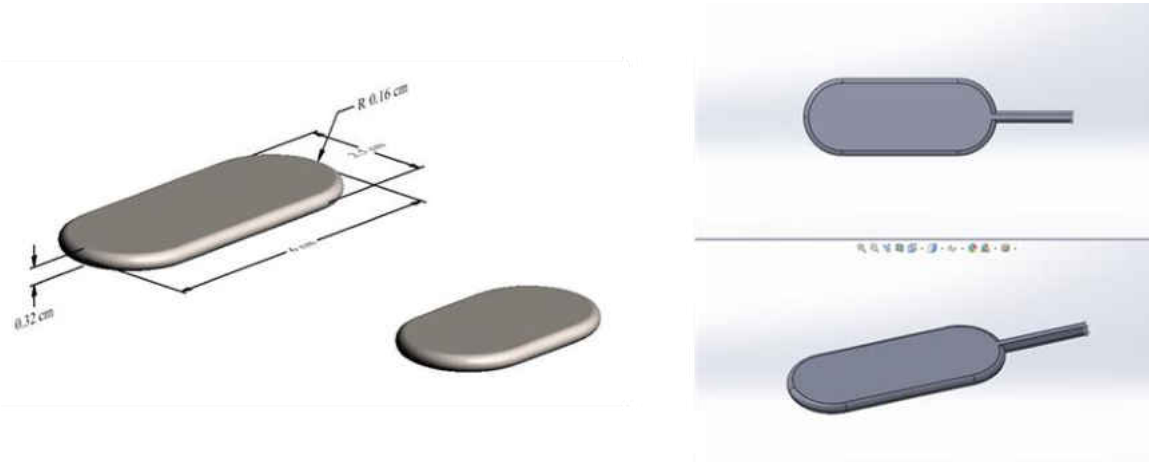


**Figure 2-17: First Single Electrode Design**

The test electrode was fabricated at the CATER machine shop out of an aluminum block. As shown

on the left-hand side of Fig. 2-18, the test electrode was roughly 5 cm (2 in) in length and 2.5 cm

(1 in) in width. The thickness of the electrodes was 0.32 cm (1/8 in). The rod extending from the

flat surface of the electrode was 0.3175 cm (1/8 in) in diameter and 5 cm (2 in) in length. The test

electrode was mounted and tested in the SBF, as shown in middle of Fig. 2-18. The test Mach

number was set at 1.75 with ± 0.1. The ± 0.1 uncertainty on the Mach number derived from

measurements of the Mach wave angle done through image processing. The electrode was not

powered for the structural test. The goal of the test was to determine the structural integrity of the

test electrode. On the right-hand side of Fig. 2-18, it was shown were the test electrode failed. The

failure was caused by excessive flutter and eventual yield of the aluminum material at the

connection between the mounting rod and the flat surface of the electrode. All future electrode

designs were analyzed through the use on FEA software package in SolidWorks before the structural test were done.



**Figure 2-18: Test Electrode Wind Tunnel Test**

Due to the failure from the first test electrode it was decided that a stronger material was needed for the electrode. The material chosen was 304 SS, which was relatively easy to machine and provided a much higher modulus of elasticity, *E*.

The next series of iterations in the design of the electrode reduced the surface area, rounded the corners with a larger radius and increased the thickness of the electrode. The surface of the electrode shrunk from 5 cm x 2.5 x cm to 4 cm x 2 cm. Resulting in a decreased wetted area of the electrode, therefore decreasing the aerodynamic forces on the electrode. The thickness of the electrode was increased from 0.32 cm (1/8 in) to 0.64 cm (1/4 in) which provided a stiffer attachment rod and flat plate to avoid flutter issues. The left-hand side of Fig. 2-19, shows a design with the addition of the larger diameter rod. The next iterations of the electrode design are shown on the middle and right-hand side of Fig. 2-19. These had rounder and thicker electrode that transitioned with the rod diameter.
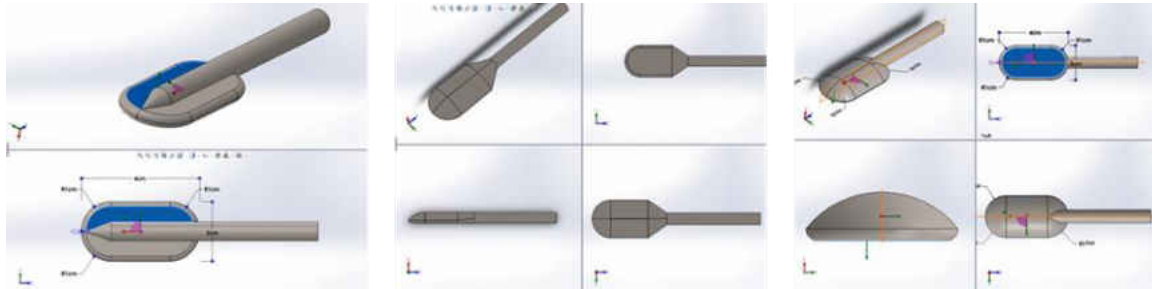
**Figure 2-19: Electrode Design Iteration with Larger Diameter Rod**

This design was meant to be stronger and smaller to assure that it could with stand the aerodynamic forces. A preliminary FEA, illustrated in Fig. 2-20, shows that the design could withstand the aerodynamic forces equivalent to 25 psi. The dominating aerodynamic force on the electrode would be a negative lift force. The 25 psi on the bottom surface simulated a negative lift force. The maximum deflection for the design was approximately 0.113 mm, which was considered acceptable.
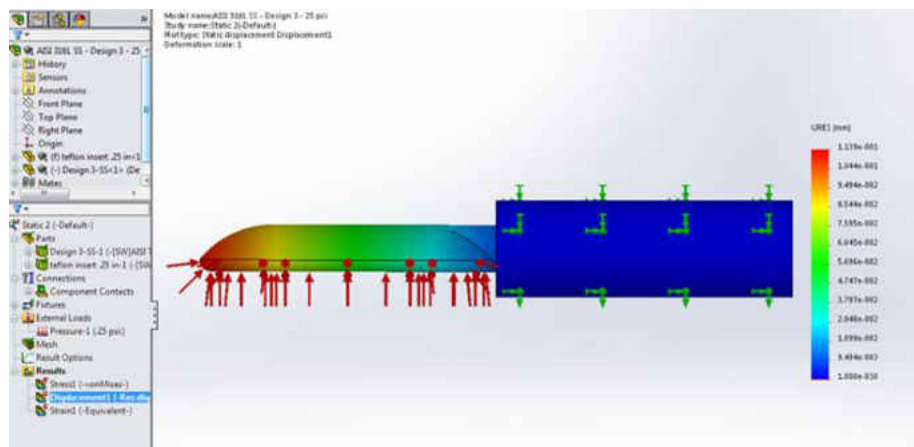


**Figure 2-20: FEA of Larger Diameter Rod Electrode Design at a Load of 25 psi**

The electrode design at this point was reviewed with the electrostatics SME's at ESPL. The design required more blended corners and larger radii along the edges. Therefore, the next series of

iterations traded more heavily on the electrostatic and aerodynamic properties of the electrode. The transition between the extruding rod and the electrode surface were considered high electric field concentration points. The left-hand side of Fig. 2-21, illustrated the more rounded design which satisfied the electrostatic properties for the design. However, after some analysis it was determined that the design became highly 3-dimentional and could cause more complicated shock structures. The rounder and blunter leading edge would lead to a stronger bow shock, which was not desired. Additionally, the thickness of the design was twice of the original design which also contributed to a stronger bow shock.

The next iteration with a more aerodynamic electrode are shown in the middle and right-hand side of Fig. 2-21. The leading-edge thickness had been reduced to half (0.32 cm) and have a linear transition to the thickness were the rod met the flat surface. This trade off made the electrode more wedge shape which is favorable for the aerodynamics, while keeping the rounded leading edge. The leading edge was also made more 2-dimentional by reducing the curvature of along the span of the leading edge from 1 cm to 0.16 cm. This design also simplified manufacturability, which reduced the cost and lead time.
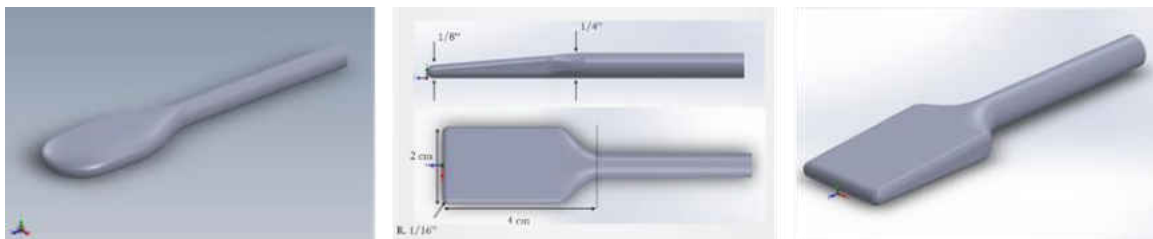


**Figure 2-21: Electrode Design with Rounder Corner and Larger Thickness**

A quick FEA simulation utilizing SolidWorks was performed on this design. The aerodynamic negative lift force was set at 150 psi. Based on the previous calculation of the worst scenario the maximum aerodynamic force expected for the Mach 2 flow was 130 psi. Therefore, the 150-psi simulation had a safety factor of 1.15.

Figure 2-22, illustrated the results of the SolidWorks FEA simulation. The FEA showed a maximum deflection at the leading edge with a magnitude of 0.366 mm. The minimal deflection is desired to avoid exceeding the yielding strength of the material and potential flutter effects. As a preliminary FEA analysis this was considered an acceptable result to move on to fabricating a test electrode with this design.
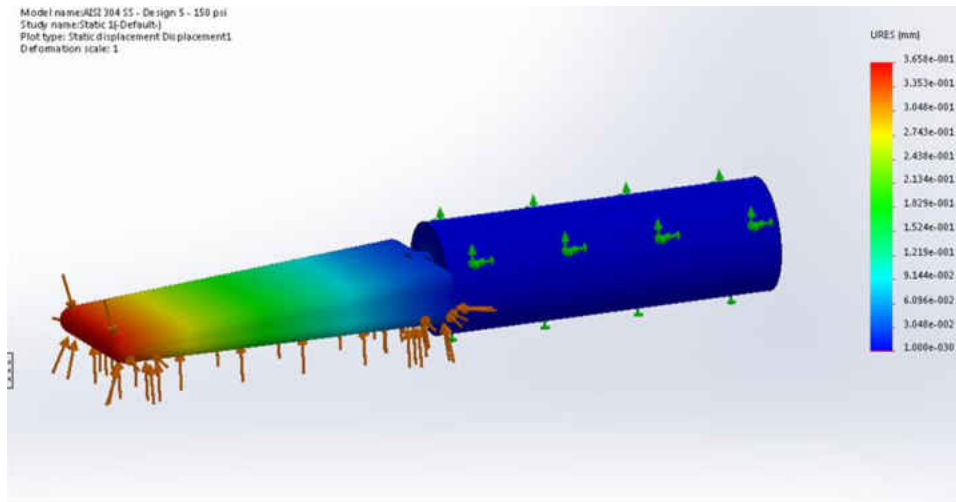


**Figure 2-22: FEA of Electrode Design with Rounder Corners at a Load of 150 psi**

The test electrode was fabricated at the CATER machine shop. It was manufactured from a of 304 SS bar and to a 4/5 scale. In the design model the electrode surface was 4 cm x 2 cm x 0.64 in length, width and thickness, respectively. With the leading edge starting at a thickness of 0.32 and linearly increasing to 0.64 cm at the end of the electrode surface. The rod diameter was 0.64 cm

and was 4 cm long. After fabrication the test electrode actual dimensions were 4 cm x 1.93 cm x 0.53 cm, in length, width and thickness respectively. The leading edge tapered from 0.30 cm to 0.53 cm. The rod diameter was 0.53 cm and 4 cm in length. Figure 2-23, shows an illustration of the test electrode. It was inserted in the PTFE sleeve as shown in middle of Fig. 2-23. Then it was inserted into a copper sleeve and then the sting mount, as shown in right-hand side of Fig. 2-23.
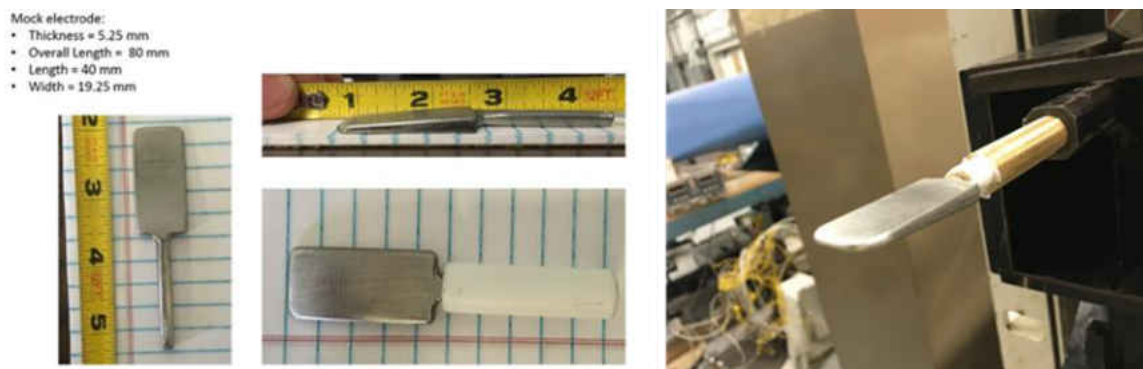


**Figure 2-23: Test Electrode of Rounder Corner Design**

The structural test of the electrode at Mach 2 was successful. The electrode did not experience any noticeable flutter and the measure deflection was less than 1 mm. The result showed that the design can meet the structural criteria. The next step was to examine the aerodynamic characteristics of the test electrode and tunnel interface to assure that the flow would remain supersonic between the gap.

Schlieren imaging was used to examine the shock interactions between the electrode and the tunnel. The schlieren set up will be described in detail in the experimental setup section of Chapter 3. Figure 2-24, shows the test electrode under at Mach 2.7. An approximate tolerance of +/- 0.1 on the Mach number was found by using the measured Mach wave angle in the images.
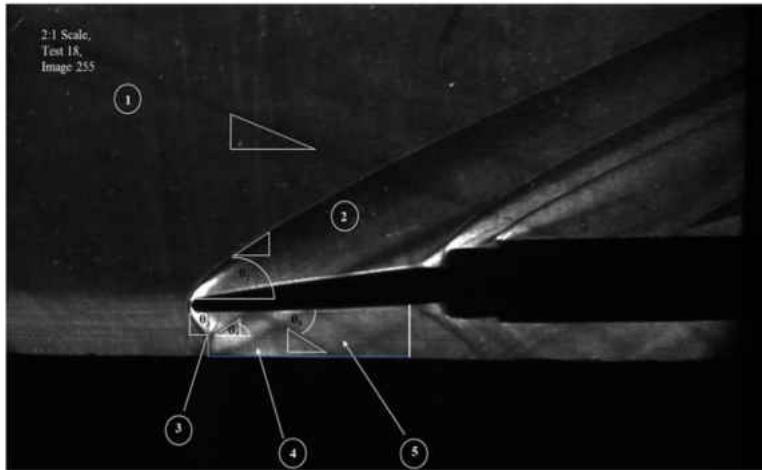
**Figure 2-24: Aerodynamic Test of Rounder Corner Electrode Design at Mach 2.7**

Figure 2-24, illustrates a series of shock reflections within the gap of the electrode which indicates that the flow in the gap was supersonic. A slight angle of attack was noticed on the electrode which was address in the final design by machining the PTFE insert to a higher tolerance.

The CAD and engineering drawings for the final electrode design are shown below in Fig. 2-25. The final design included a rounder leading edge which increased the curvature from 0.16 cm to 0.32 cm. This modification was done to avoid a high electric field concentration point at the leading edge, as suggested by the electrostatic SMEs at ESPL. Other than that modification, the design remained the same as the one that was tested during the last iteration.
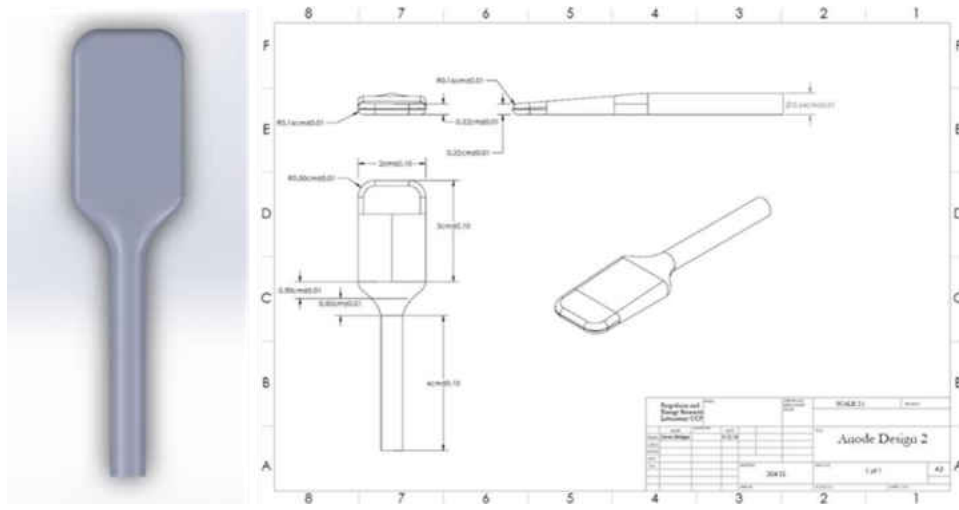
**Figure 2-25: Final Electrode Design and Engineering Drawings for Manufacturing**

Figure 2-26 shows several views of the final manufactured electrode. The surface was polished to a mirror-like finish to avoid electric field concentration points due to the surface roughness. The PTFE sleeve is pressure fitted in the cooper sleeve.
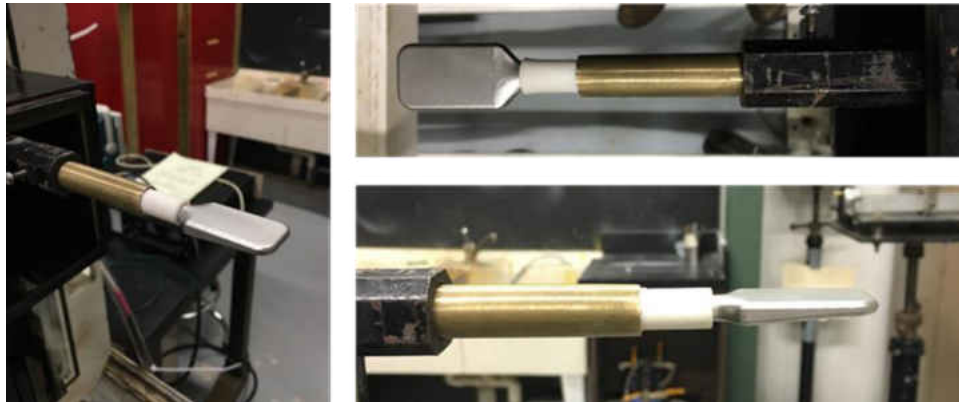


**Figure 2-26: Final Electrode Manufactured and Mounted on Sting Mount**

The left-hand side of Fig. 2-27, shows the back side of the electrode which tapped to mount a screw for the HPVS connection. A 40-kV rated PTFE wire was connected to this screw to provide

the high voltage. The wire was fed through the sting mount and out of the top side of the test facility. The right-hand side of Fig. 2-27, shows the PTFE sleeve, which extended 4 cm past the electrode rod to assure that the connection was insulated from the outer copper sleeve. The PTFE sleeve was machined at the UCF machine shop to achieve a straighter fit. The copper sleeve provided structural support for mounting purposes.



**Figure 2-27: Final Electrode Design HVPS Attachment and PTFE Insulation**

The top of Fig. 2-28, shows the schlieren image of the final electrode under a Mach 2.7 flow. In this image the electrode is traversed 2.0 cm away from the top inner wall of the tunnel test section. This test was similar to the previous test electrode aerodynamic test, shown in Fig. 2-24.

Another structure that was shown in Fig 2-28, was a Mach reflection. The Mach reflection has three trunks. The first trunk is an oblique shock (incident shockwave), the second trunk is a normal shock and the third trunk is a reflection shock. These Mach reflections occur when the blockage is great enough to induce a partial normal shock in the flow. This is also typical behavior of lower Mach numbers. The 2.0 cm gap created enough blockage to cause the Mach reflection at a free stream Mach of 2.7 [25].

Even though the gap experienced a Mach reflection which cause significant decrease in the Mach number, the flow remained supersonic. Therefore, it was determined that the electrode met the aerodynamic criteria of the design. The successful structural and aerodynamic test indicated that the design was acceptable. This was the electrode used for experimentation. Figure 2-28, also shows the streamline of the flow through the incident shockwave and the reflected shockwave which are both followed by a Prandtl-Meyer expansion due to the turn angle induced by the shockwaves.
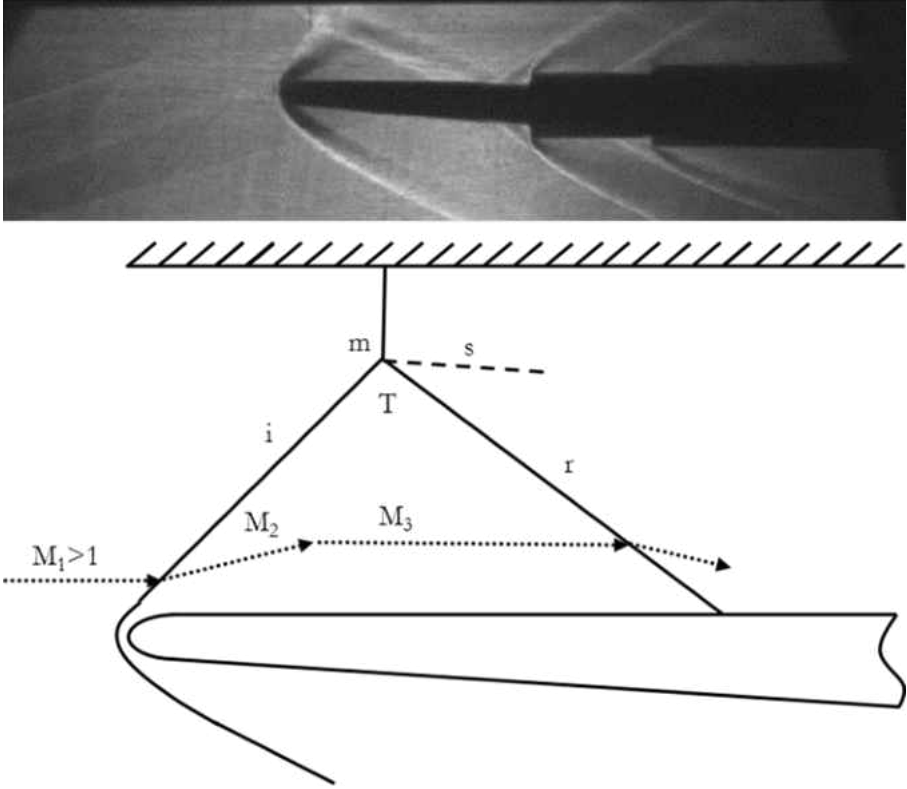


**Figure 2-28: Wind Tunnel Testing of Final Design at Mach 3.2**

## 2.5      Summary

The theoretical Paschen's law, which accounts for aerodynamic effects explained in this chapter. A theoretical model that accounts for compressible flow effects and flow velocity was re-derived. This was the theoretical model that requires data for validation. The requirements of the data were discussed. The data must contain Mach number, pressure measurements and gap height to be plotted on the Paschen's law graph. The electrostatic properties can be calculated for the material and maximum radii of the geometry. Therefore, if the Mach number, local static pressure and gap width are known the theoretical voltage can be calculated. An experiment that can gather such data was required for this research activity. The following chapter will discuss the experimental set up and an analysis of the results.

# CHAPTER 3: EXPERIMENTAL RESULTS AND ANALYSIS

## 3.1 <u>Introduction</u>

This chapter contains an explanation of the experimental set up and results. It expands on the results and analysis of the behavior of the supersonic flow and electrostatic interactions. The objective of this research initiative was to investigate how supersonic flow influences the discharge voltage dictated by the theoretical Paschen's law model that was developed. To achieve an understanding of this effect on must also understand how the ESD affects the supersonic flow because this will affect the measurements that were gathered. Therefore, some literature review was required to understand what others have found in interactions between supersonic flow and ESD events.

Ernst Mach was the first person to observe a spherical shockwave from an ESD event using schlieren imaging, as shown in Fig. 3-1. The shockwave that he observed was emanating from a spark. He followed this work with the development of gas dynamics relations. Throughout his work in characterizing shock waves he noted that the fluid intensive properties such as temperature and pressure changes as the shock wave moved in the medium. To be more specific he noted that the temperature and pressure would rise across a shock wave [16]. Anyone that has studied compressible flows is now very familiar with the changes in intensive properties across a shock wave. This will be the fundamental physics of the experiment conducted during this investigation.

Other works investigating electrostatic discharges in supersonic flows have found that shockwaves can be controlled and produced by ESD events. Three major effects have been found to dominate this process. Those effects are electrostatic forces (on particles), magnetohydrodynamic forces,

and heat addition by thermal energy release from the plasma of the ESD event. However, all three of these effects have found to have an influence on the supersonic flow at high power levels. The power level for the ESD events that have been found to control the flow are in the order of *3 kW - 17 kW,* these effects are shown in Fig. 3-2 [4]. The experiment presented in this work used power levels of around *52 W*, which means that they are two order magnitude less than the power need to produce the shock control effects. It was determined that it would be more likely that shockwaves emanated from the sparks at close proximity and some thermal energy can affect the pressure measurements.

A Mach 1.7 facility was used for this investigation. A custom designed 304 steel electrode and the supersonic wind tunnel steel wall were used to create ESD events on and near the surface of the static pressure ports to investigate the variations in the measurements. The energy deposition was held constant at *52.5 W*. A fully conditioned pressure transducer was installed to capture pressure variations. A PCB transducer with up to *150 kHz* sample rate capabilities was used to gather the static pressure measurements along the wall across the charged electrode. A dimmed schlieren flow visualization technique that properly captures sparks from ESD was used to observe the interaction of the ESD events with the supersonic flow [3]. The appropriate technique to capture the ESD event required low light source intensity, low amounts of stray light and very low exposure. The ratio and standard deviation between pressure measurements with and without ESD events has been quantified and recorded in this work.
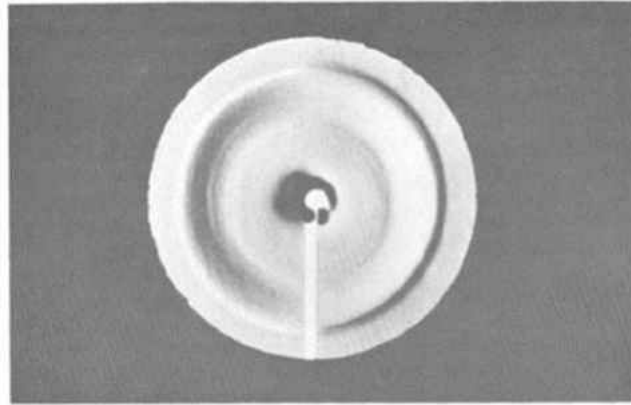
**Figure 3-1: Ernst Mach Spark Imaging with Toeplers Schlieren System**

Source: Reichenbach, H. "Contributions of Ernst Mach to Fluid Mechanics." Annual Review

Fluid Mechanics, 1983, pp. 1–29., Accessed 1 Mar. 2017.



**Figure 3-2: Magnetohydrodynamics and Thermal Effects of Plasma in Supersonic Flow**

Source: Sergey, Leonov, Dmitry, Yarantsev , Alexander, Kuriachy, and Victor, Soloviev.

"Supersonic/Transonic Flow Control By Electro-Discharge Plasma Technique" 25th

International Congress Of The Aeronautical Sciences, Hamburg, Germany, Sept. 3-8, 2006.

## 3.2    Experimental Set Up

### 3.2.1    Hardware

#### 3.2.1.1 Electrode Placement

The blowdown supersonic wind tunnel at the Center for Advance Turbomachinery and Energy Research at the University of Central Florida, Orlando was employed to provide t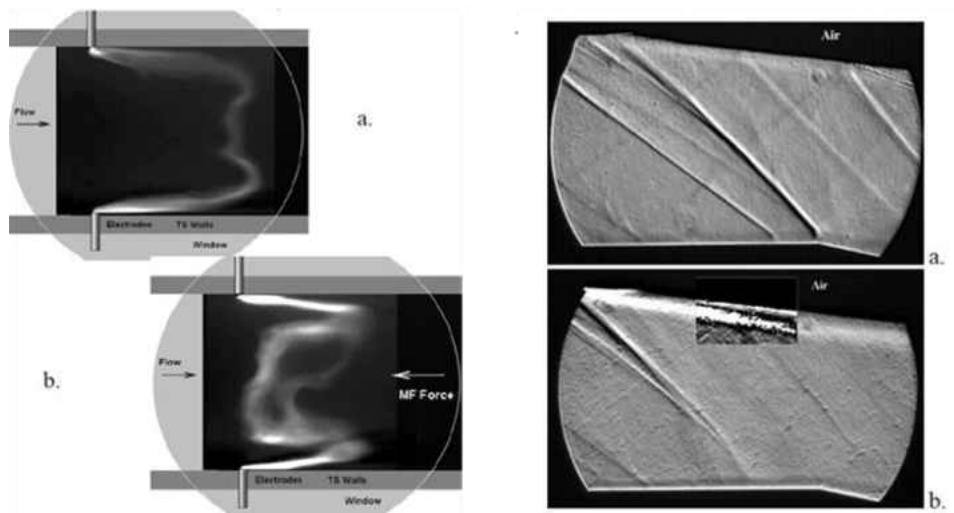he supersonic flow. The custom designed 304 stainless steel electrode was connected to a 60 kV high voltage power supply to create the ESD event. The electrode was installed at a set distance from the top plate of the test section and acted as an anode with the wall acting as the cathode, shown in Fig. 3-3. The Mach number of the wind tunnel was varied between 1.3 to 3.5 to find the optimal Mach number that would influence the ESD event and yet allow for ESD events to occur during a quasi-steady supersonic flow. The optimal Mach number for this configuration was 1.7. Therefore, a constant Mach number of 1.7 was used throughout this investigation. Mach number measurements can fluctuate as much as $\pm$ 0.1 depending on the image quality, because the Mach number was measured from the Mach waves in the schlieren images. One pressure port was instrumented with a fully signal conditioned pressure transducer and the other one was instrumented with a PCB Piezotronic pressure sensor, which required active in-line conditioning. The transducers are not intended to gather the same pressure but rather to compare the reaction of the two sensors.
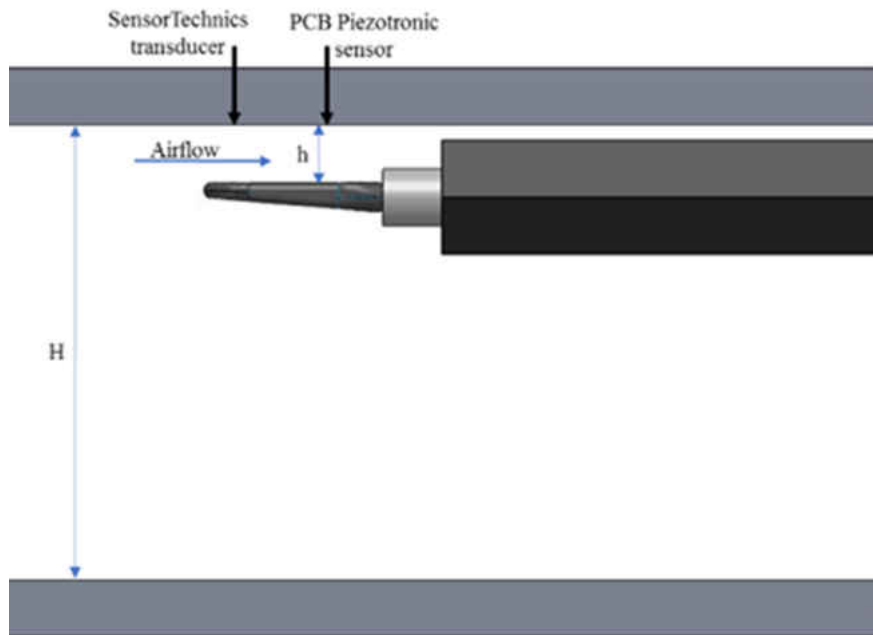
**Figure 3-3: CAD of Electrode Placement in Test Section**

The stagnation reservoir had a volume of 18.9 m$^3$ and maximum stagnation pressure of 18.6 bar. The test section cross-section was 10.12 cm in width by 10.12 cm in height, as shown in Fig. 3-3. A sting mount held the electrode in place at h = 1.3 cm from the top plate. Under supersonic flow, the electrode deflection was measured to be ± 3.97 x 10$^{-2}$ cm.

The wall of the wind tunnel acted as the cathode and the electrode mounted on the sting mount acted as the anode. The electrode mounted on the sting mount, the anode, was custom design to optimize its aerodynamic and electrostatic characteristics as described in the previous chapter. The aerodynamic requirements called for a slender and sharp body which would allow supersonic flow to continue throughout the length of the gap. The electrostatic requirements called for a smooth surface with no sharp corners which would have a more uniform electric field and thus favor an

ESD to happen perpendicular to the flow and avoid a premature ESD event caused by high electric field concentration around sharped corners. After many design iterations and finite element analysis of the anode an optimal design was achieved. The design had no sharp edges and therefore no points of high electric field concentration. The 304 SS material was specifically chosen over an aluminum because the strength allowed for a slender body which could withstand the aerodynamic forces of the supersonic flow. Thus, it was possible to create a slender and smooth anode which had favorable aerodynamic and electrostatic characteristics. The anode was polished to a mirror-like finish to avoid any electric field concentration in the scratches and digs from machining. A significant amount of effort during this investigation went into the anode design as it required many iterations and trial runs to test its structural strength and observed its aerodynamic characteristics through schlieren imaging.
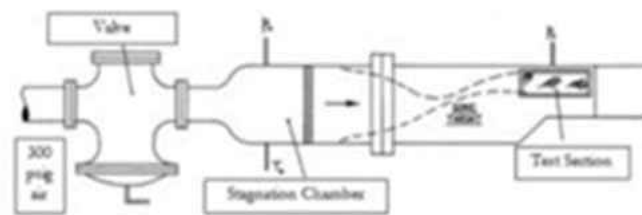
3.2.1.2 <u>Supersonic Wind Tunnel</u>



**Figure 3-4: Image of Supersonic Wind Tunnel at CATER**

Figure 3-4, shows an image of the CATER SBF. The facility uses a wide-angle diffuser and a series of screens to straighten the flow. Then it processed to a shaping section which transitions the circular cross section into a rectangular cross section that matches the converging-diverging (CD) nozzle inlet. The CD nozzle is made of two thin SS plates which sit on top of several jack-like actuators that are controlled manually through a crank on the top of the tunnel. The CD nozzle and test section are on one continuous SS plate; therefore, a smoother flow can be achieved at the test section. The facility has a larger second throat downstream of the test section that acts at the diffuser for the facility. This blockage throat allows for longer run times by diffusing the flow

through a series of oblique shocks as opposed to a single normal shock. The then exhausted the flow into ambient conditions outside of the building.

3.2.1.3 Static Pressure Transducer and Dynamic Pressure Sensor
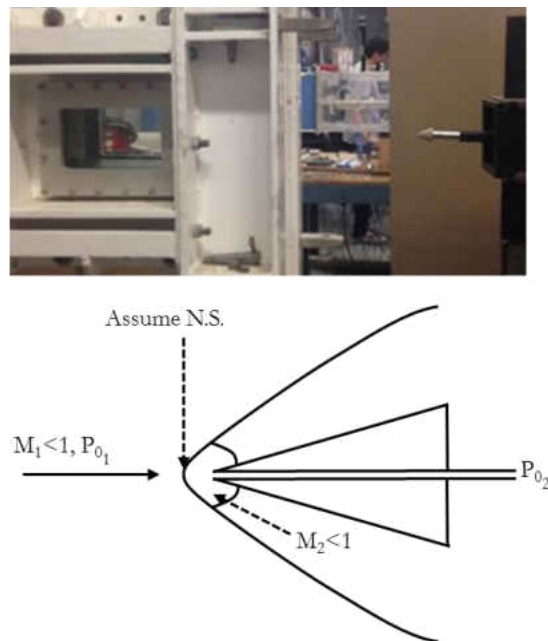


**Figure 3-5: Stagnation Pressure Measurement Technique for Supersonic Flows**

As illustrated in Fig. 3-5, the stagnation pressure in the freestream flow can be approximated by assuming an infinitesimal normal shock upstream of a blunt stagnation pressure probe. For these measurements a 30-degree cone was used as the stagnation pressure probe.

$M_1$ and $P_{02}$ are values obtained through visualization measurement and pressure gauge, respectively. Assuming there was an infinitesimal normal shock just upstream of the pressure probe the following calculations can be done to calculate $P_{01}$

From normal shock relations [20]

$$P_{01} = \frac{P_{02}}{\left[\frac{(\gamma+1)*M_1^2}{(\gamma-1)*M_1^2+2}\right]^{\frac{\gamma}{\gamma-1}} * \left[\frac{(\gamma+1)}{2*\gamma*M_1^2-(\gamma-1)}\right]^{\frac{1}{\gamma-1}}} \tag{33}$$



**Figure 3-6: Test Section Addition for Pressure Sensor and Transducer Instrumentation**

Source: Hogue, Michael, D., Cox, Rachel, E, Mulligan, Jaysen, Kapat, Jayanta, Ahmed, Kareem,

Cox, Rachel, E., Wilson, Jennifer, G., and Calle, Luz, M. "Revision of Paschen's Law Relating

to the ESD of Aerospace Vehicle Surfaces" Proc. 2017 Electrostatic Joint Conference,

University of Ottawa, June 13-15, 2017.

The electrostatic discharge events were produced by a Glassman High Voltage power supply. It

provided a nominal input power of 52.5 W at 35kV and 1.5 mA. This was sufficient to cause rapid

ESD events with no flow and occasional ESD events with nominal Mach 1.7 flow. A Tektronix 4

channel digital oscilloscope was used to record the voltage and current output of the high voltage

power supply.

The SensorTechnics transducer was a fully conditioned pressure transducer (Model: HCX002A6V) which was supplied with an excitation voltage of 5.5 V. It provided measurements with an uncertainty of ±5 mbar. This transducer was directly connected to a BNC rack. Since it was fully conditioned it did not require any further in-line conversions. A calibration was performed to find Eq. 34, which translate voltage to pressure.

$$P = 329.2 * V + 1.21 \text{ [Torr]} \tag{34}$$

The second pressure transducer was a PCB Piezotronics high sensitivity pressure sensor (Model: 176M11) with an uncertainty of ±1%. The PCB sensor connected to in-line differential converter (model 422M182) with a sensitivity of ±5% using a low noise cable. The converter was then connected to a PCB charged signal conditioner (Model: 482C54) with an associated uncertainty of ±5%. The signal conditioner then sent the signal to a National Instruments BNC rack. The data was recorded from the BNC rack by a PCI 6221 card. A LabVIEW VI was created to record the input from both pressure transducers. The in-line conversion for the PCB transducer followed these equations. The PCB Piezotronic sensor sensitivity is;

$$S_{PCB\ sensor} = 859.5 \ [\frac{pC}{Torr}] \tag{35}$$

The in-line converter sensitivity is;

$$S_{converter} = 4 \ [\frac{mV}{pC}] \tag{36}$$

Finally, resulting in the signal into National Instruments PCI 6221 card which relates voltage and pressure as follows;

$$Signal_{PCB\ Sensor} = S_{PCB\ sensor} * S_{converter} = 3438 \left[\frac{mV}{Torr}\right] \qquad (37)$$

Equation 37 was used to convert the voltage input from the PCB sensor to a pressure reading. The sampling frequency was set to 125 kHz to properly sample the flow. The sample size varied from 8,500-16,000 samples per run. The standard error mean for the HXC002A6V transducer was calculated to be $\pm 1.8 \times 10^{-3}$. The standard error mean associated with the PCB transducer data was $\pm 1.1 \times 10^{-3}$. The pressure sensor and transducer were mounted on the added test section shown in Fig. 3-6.
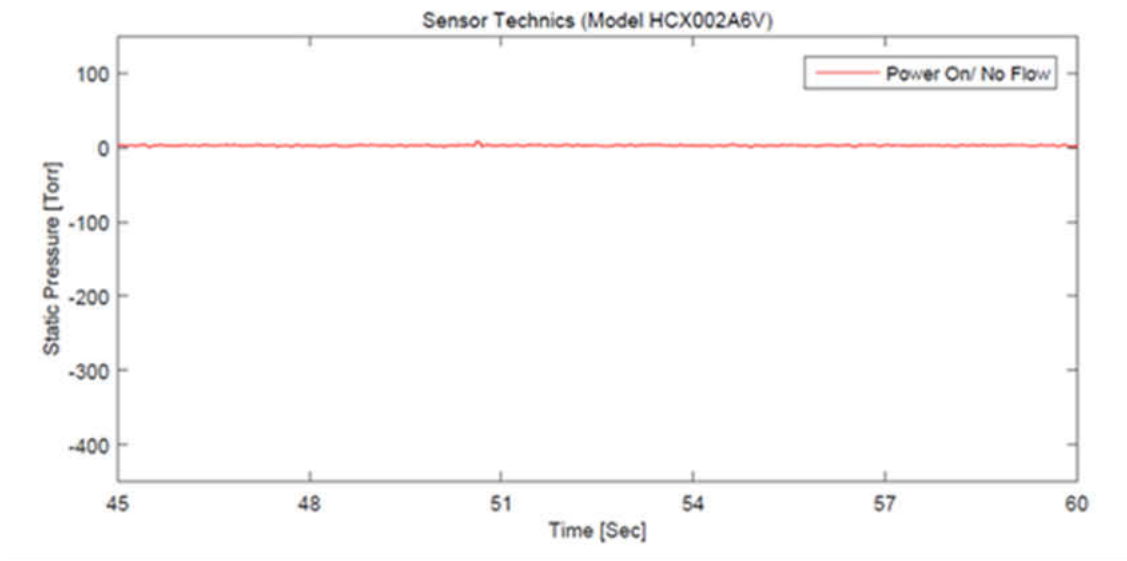


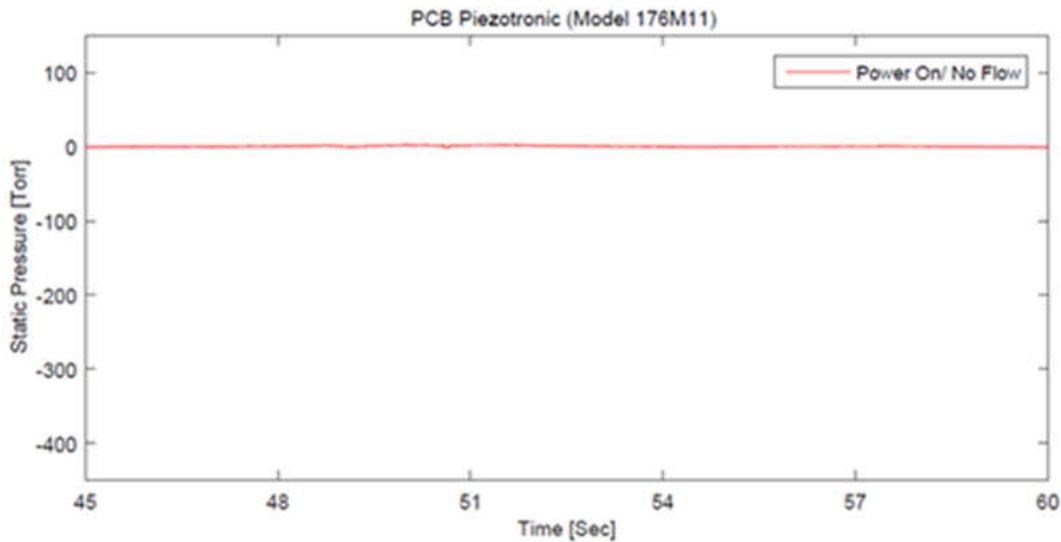**Figure 3-7: Static Pressure Transducer Test for Noise from Sparks**

**Figure 3-8: Dynamic Pressure Sensor Test for Noise from Sparks**

Figure 3-7 & 3-8 were two cases performed under a no flow and power on (i.e. ESD events manifesting) condition. This was done to ensure that the instruments readings were not influenced by any electrical noise that could arise from the ESD events. Precaution were taken to ensure that the instrument would not come in direct contact with the ESD events. Furthermore, low noise electrical wires were used to connect the sensors. It was clear that the electrical noise from the ESD events did not influence the reading of the pressure sensors.

3.2.1.4 Schlieren Imaging System and Experiment Schematics

A Z-type schlieren system was used as the method for noninvasive flow visualization. The optical system consisted of two spherical Edmund Optics six-inch mirror with a 60-inch focal length. A 150-Watt halogen optical system was used as the light source. A straight knife edge was used to cut the light at the focal point of the second mirror to create the schlieren effects. A Vision

Research, Phantom v5.01 high speed camera was used to capture the image at an exposure of 10-100 μs, 800-1600 fps, and a resolution of 512 x 512 pixels. The optical set up is shown in Fig. 3-9.
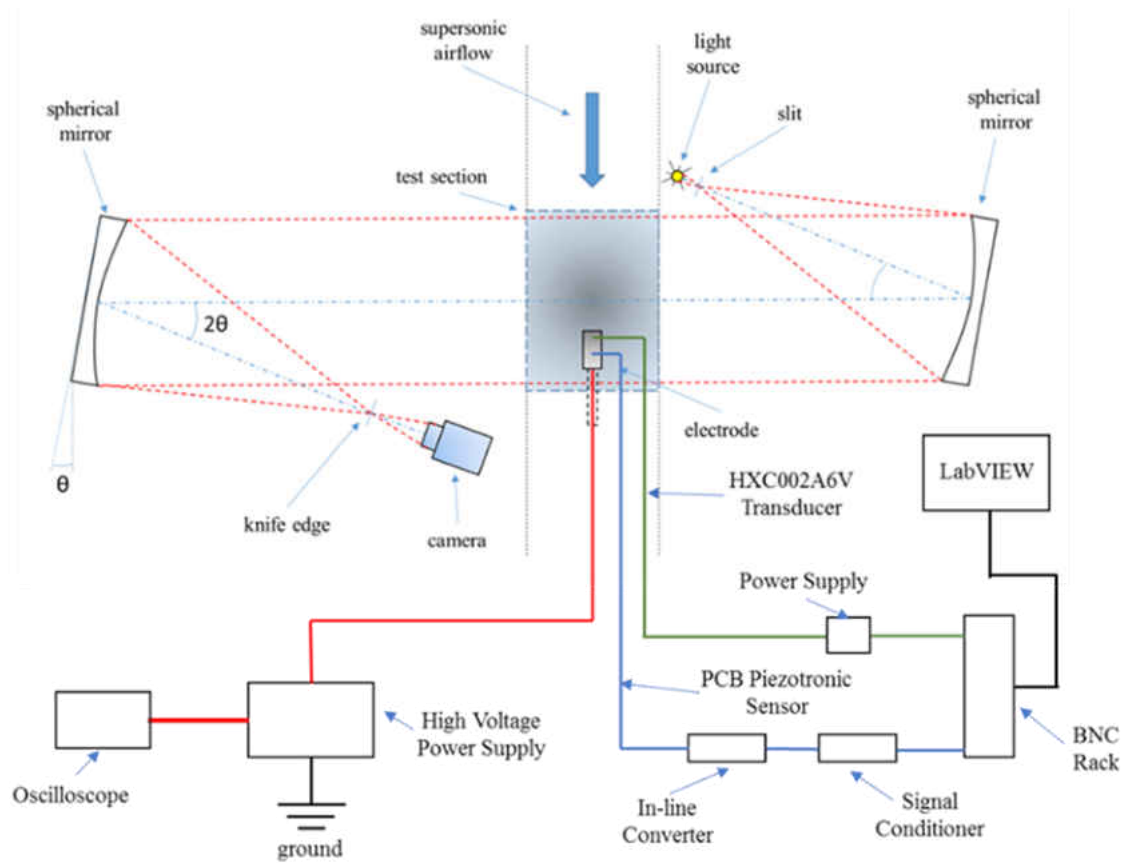


**Figure 3-9: Schlieren Imaging System and Experiment Schematics**

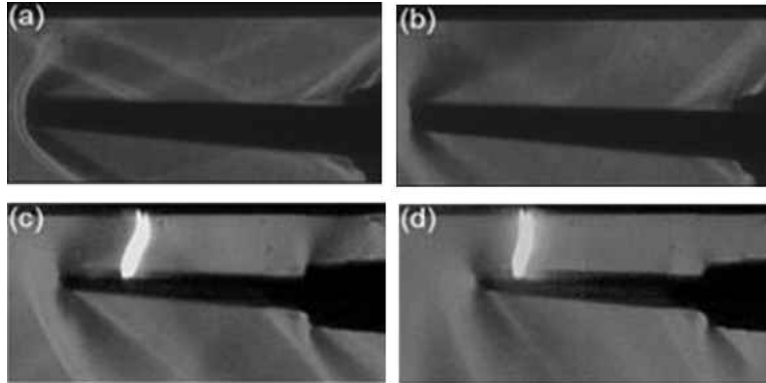3.2.1.5 <u>Electrode and Shock Interactions</u>

3.2.1.5.1      Flow in the Gap



**Figure 3-10: Electrode Discharge Location**

**Table 3-1: Flow Conditions and Run Times**

| Figure | Condition | Duration [sec] | Comments |
|--------|-----------|----------------|----------|
| (a) | Steady | ~8 | Baseline shocks |
| (b) | Transient | ~2 | Baseline transient |
| (c) | Steady | ~8 | ESD event |
| (d) | Transient | ~2 | ESD event |

The electrostatic discharge events were observed during two distinct flow conditions. The conditions were quasi-steady supersonic flow and a transient shock train, shown in Fig. 3-10 (a) & 3-10 (b), respectively.

Less sparks occurred during the quasi-steady supersonic flow. This correlates with theoretical work which indicates that supersonic flow will quench rapid sparking [22]. Frequent sparking was observed during the shock train. These conditions were consistent throughout all the scenarios.

The quasi-steady supersonic flow maintained a bow shock at the tip of the electrode. The Mach number across the bow shock can be estimated by using oblique shock and Prandtl-Meyer expansion fan relations [20]. The free stream Mach number was 1.7 and the Mach number in the gap was found to be around 1.65 as well due to Prandtl-Meyer expansion that accelerate the flow back to a higher Mach number. The transient shock train was comprised of a series of oblique shocks that had been pushed downstream at the beginning of the test. However, as the pressure in the reservoir dropped below the necessary pressure to maintain the shocks downstream of the test section the oblique shocks start to move upstream. Figure 3-10 (c) & 3-10 (d) show the ESD events in the quasi-steady and shock train flow conditions, respectively. The schlieren image quality was degraded because the light source intensity had to be reduced and the camera exposure was set to 10 μs to properly capture the ESD event in the image. Table 3-1, summarizes the flow conditions.

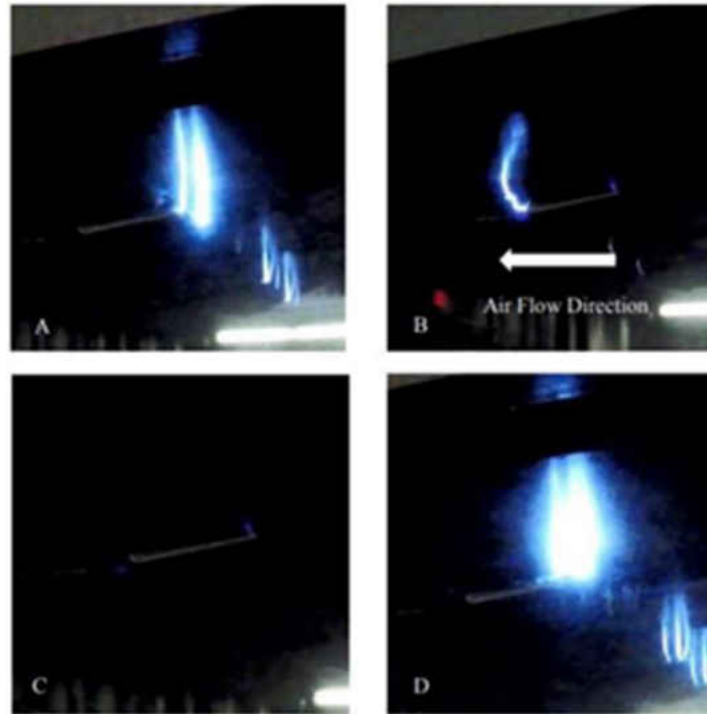3.2.1.5.2        Pressure Measurement and Electrostatic Discharge Locations



**Figure 3-11: Electrode Discharge Captured by Go-Pro Camera**

Source: Hogue, Michael, D., Cox, Rachel, E, Mulligan, Jaysen, Kapat, Jayanta, Ahmed, Kareem,

Cox, Rachel, E., Wilson, Jennifer, G., and Calle, Luz, M. "Revision of Paschen's Law Relating

to the ESD of Aerospace Vehicle Surfaces" Proc. 2017 Electrostatic Joint Conference,

University of Ottawa, June 13-15, 2017.

A Go-Pro HERO 5 camera was mounted on the side of the test section to capture the ESD events.

The perspective of the camera was able to capture the ESD event that was affected by the

supersonic flow. It is clearly visible that that flow affects the shape of the discharge path. Figure

3-11 (a), illustrates the ESD events without flow. Figure 3-11 (b), illustrates the ESD event with

flow. Figure 3-11 (c), showed the supersonic flow suppressing the ESD events. Two small regions

of higher electric field concentration points can be seen in Fig. 3-11 (c). Figure 3-11 (d), shows the ESD events after the flow was terminated.
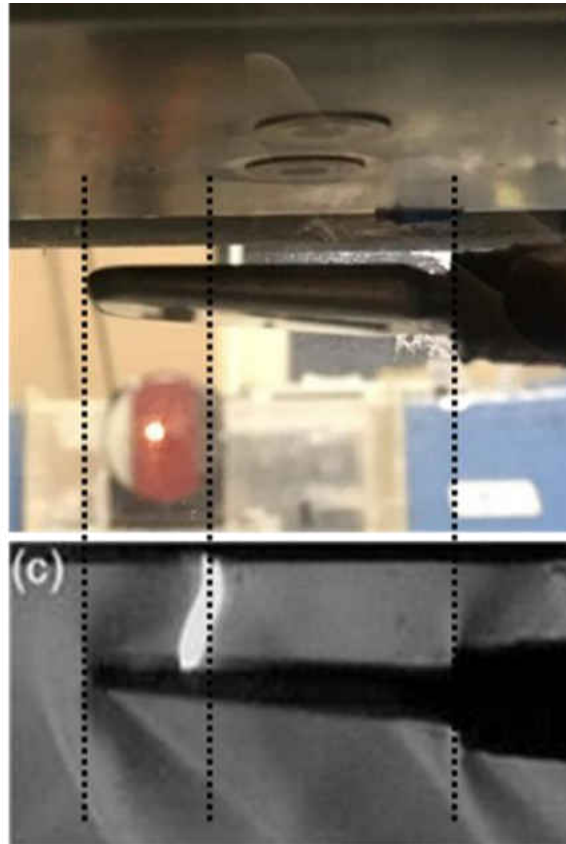


**Figure 3-12: Pressure Measurement and Discharge Location Overview**

Figure 3-12, shows the ESD event with respect to the location of the pressure sensor and transducer. The ESD event seemed to occur between both sensors. Although it is not noticeable in the still images a video recording shows that the ESD event emitted a shockwave that was able to propagate through the supersonic flow. This was suspected to cause the pressure fluctuations that were observed in the next section.

## 3.3    Results and Analysis

### 3.3.1    Pressure Trace Measurements Used for Analysis

The primary mode of flow perturbation that has been observed were weak spherical shock produced by the ESD events [16]. These interactions are manifested in a pressure change. A secondary mode of flow perturbation in this investigation is manifested through the conservation of energy principle [6]. These ESD events are highly three dimensional in nature, thus assuming a two-dimensional event would be simplistic [6]. Many studies have recorded the interaction of high energy plasma-compressed flow which can be used to produce oblique shocks in a supersonic channel flow [4-15]. The high thermal energy deposition has been linked to the formation of a virtual wedge angle which causes an oblique shock, similar to what a mechanical wedge in supersonic flow would cause. The power required to cause such strong plasma-flow interaction is two order magnitude higher than the power used for this study [5, 8]. Thus, thermal effects are assumed to have minimal influence in the pressure change recorded at the wall during this study.

Several runs were performed to insure the repeatability of the measurements. Since the measurements were very consistent, three runs were selected for analysis. Run 1 was the controlled data set with no ESD events (i.e. 'power off'). This run was used as a baseline for the two remaining runs. Run 2 was the 'power on' scenario. There were several ESD events during this run, which have been noted in Fig. 3-14 & 3-18. The power supply was on during the entire run, however the ESD manifested as short pulses affected by the flow conditions. On average the ESD event lasted approximately 5-20 ms. Lastly, Run 3b was another run without ESD events (i.e. 'power off') this run was used to compare the variation between two runs without ESD events. Table 3-2, summarizes the configuration of the runs.

Figure 3-13, contains Run 1 and Run 3b, this was the comparison between two runs without any ESD events. The pressure measurement is nearly identical for the duration of the run. Figure 3-14, contains the pressure measurement for Run 1 and Run 2. Run 2 had ESD events (in red) and Run 1 had no ESD events (in green). The change in pressure at the static pressure port for Run 2 ('power on') correlates with a local variation in static pressure induced by the repetitive shocks wave emanating from a rapid series of ESD events [5, 16].

**Table 3-2: Runs Used for Analysis**

| Test | Power | Comments |
|------|-------|----------|
| Run1 | Off | Baseline |
| Run2 | On | ESD events |
| Run3b | Off | Validation |

### 3.3.1.1 Quasi-Steady Flow Conditions

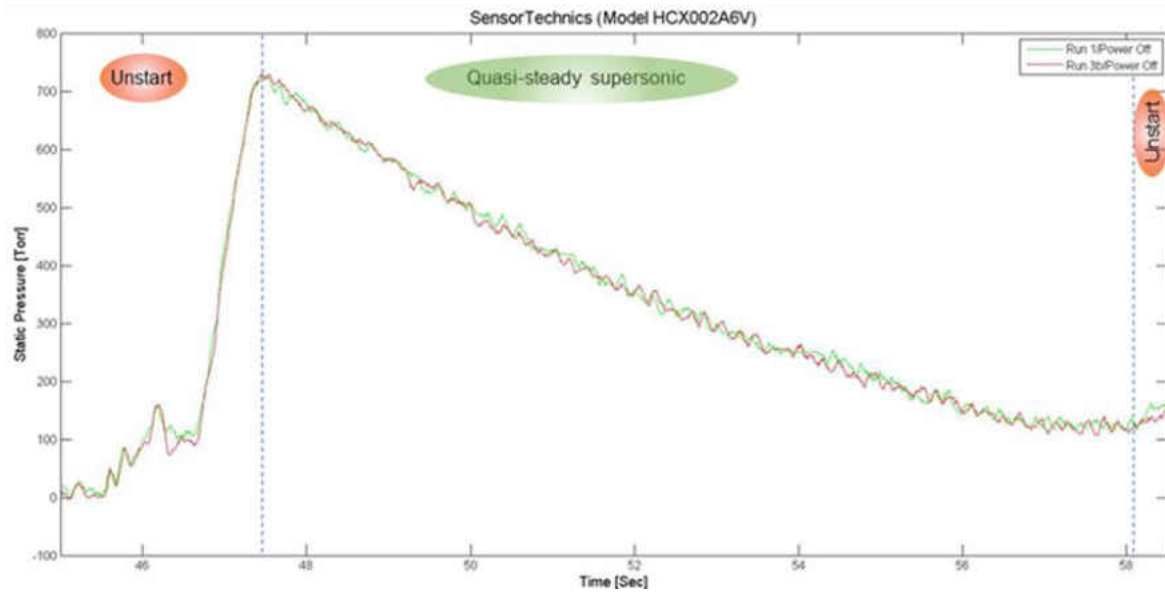### 3.3.1.1.1　Static Pressure Transducer



**Figure 3-13: Static Pressure Transducer Measurements of Test without Sparks**
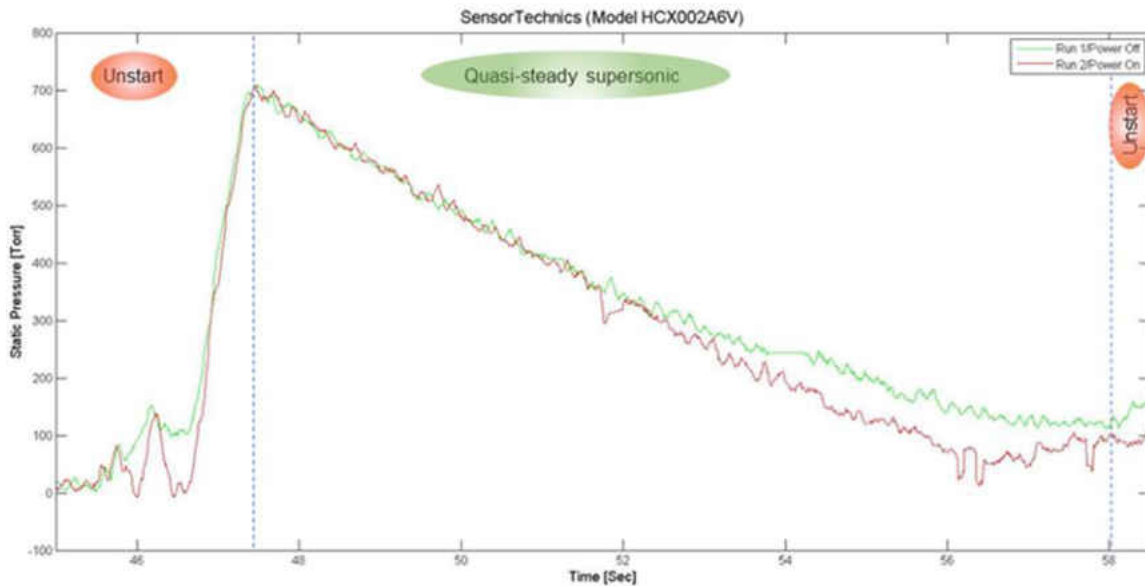
**Figure 3-14: Static Pressure Measurements of Test with Sparks**

An analysis of the ratio of the pressure traces was performed utilizing MATLAB to quantify the magnitude of variation between a scenario without ESD events to one with ESD events. Figure 3-15, shows the ratio between Run 1 and Run 3b, both having no ESD events. The result of this comparison proved the repeatability of the pressure traces. Run 3b was divided by Run 1 and plotted above the pressure traces. The standard deviation between these two runs without power was recorded to be $1.0035 \pm 7.80\%$.
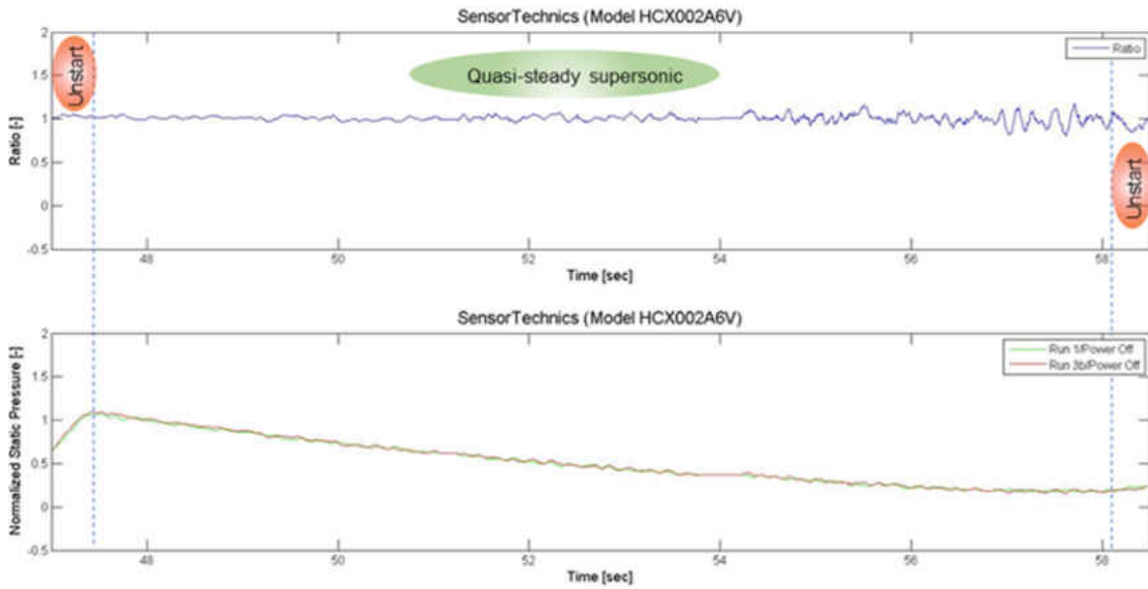
67

**Figure 3-15: Ratio of Static Pressure Measurements of Test without Sparks**

Figure 3-16, shows the ratio between Run 1 and Run 2, one without ESD events and one with ESD events.
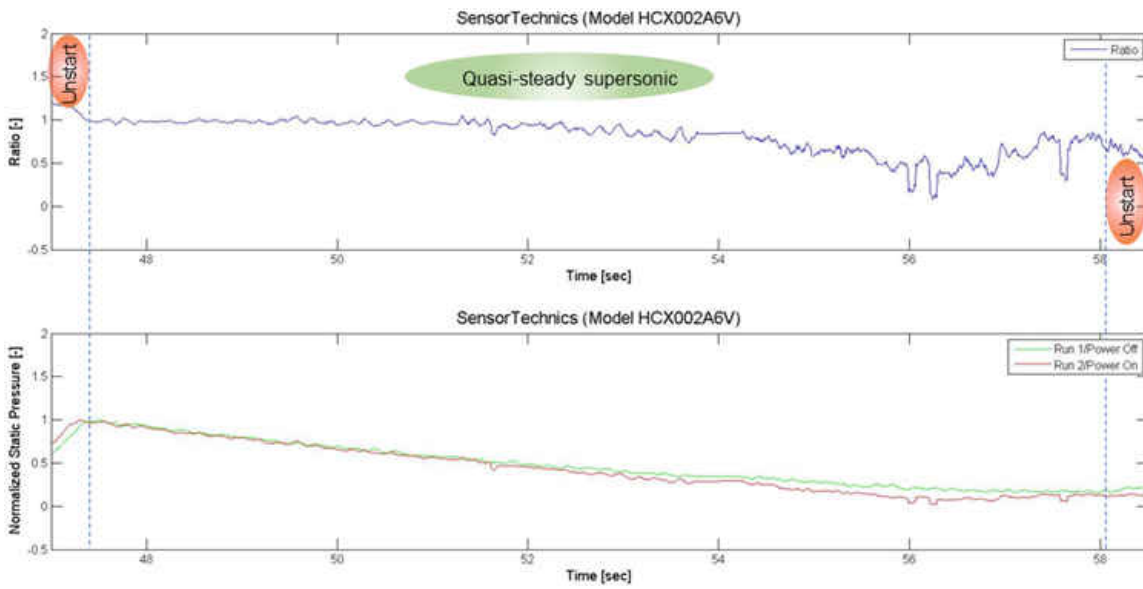


**Figure 3-16: Ratio of Static Pressure Measurements of Test with Sparks**

68

Run 2 was divide by Run 1 to plot the ratio for comparison. The $P_{rms}$ and $P'$ values for this run were calculated to be 0.854 and 1.873, respectively. This indicated a relatively large variation in pressure during the ESD events.

3.3.1.1.2    Dynamic Pressure Sensor

The same procedure for plotting and calculations were done with a PCB Piezotronic sensor. The values recorded for Run 1 and Run 3b were plotted and illustrated in Fig. 3-17. The pressure measurements are highly consistent for these two runs without ESD events. Therefore, the measurements were shown to be repeatable. Figure 3-18, shows a plot of the measurements for a run without ESD events and a run with ESD events, Run 1 and Run 2, respectively. This could be due to location of the electrostatic discharge or the characteristics of the ESD event and supersonic flow interactions.
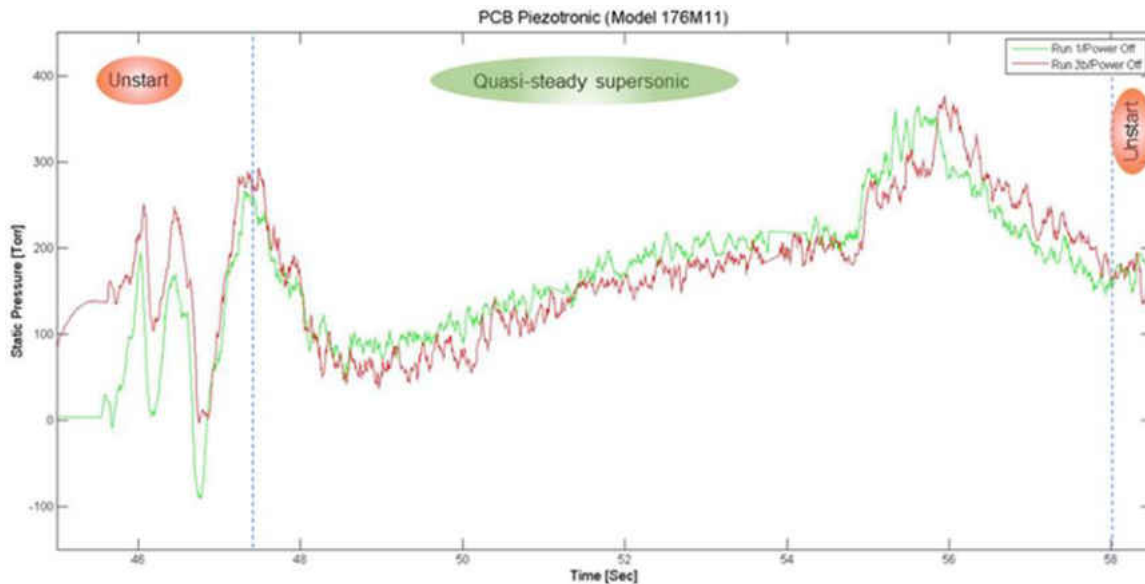


**Figure 3-17: Dynamic Pressure Sensor Measurements of Test without Sparks**
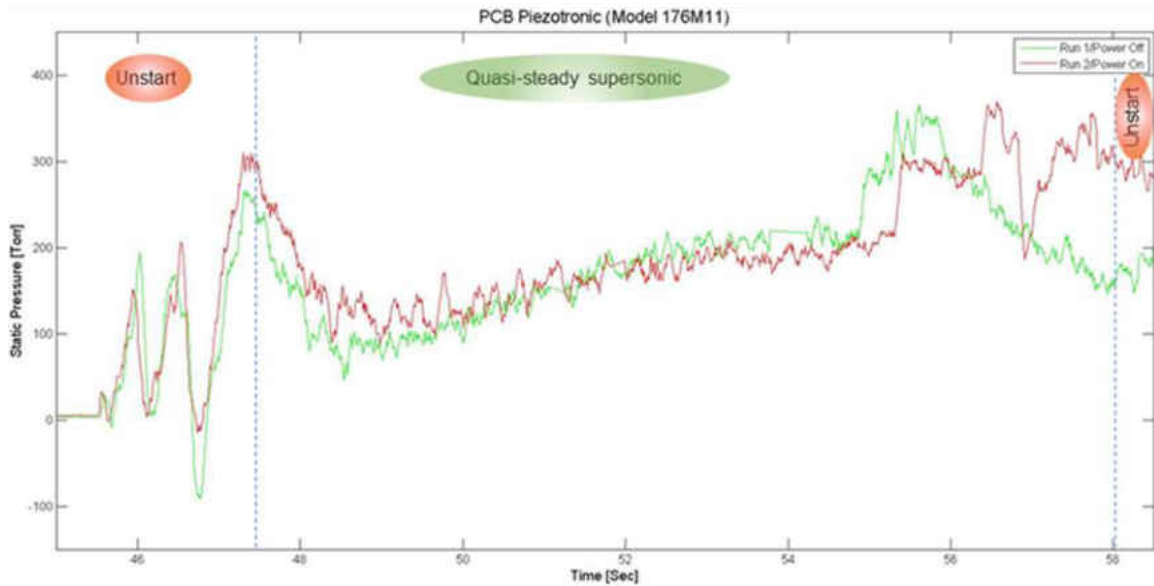
**Figure 3-18: Dynamic Pressure Sensor Measurements of Test with Sparks**

Figure 3-19, illustrates the ratio between Run 1 and Run 3b, which had no ESD events. The standard deviation in the ratio was calculated to be $1.0039 \pm 4.92\%$. These results showed the repeatability of the pressure traces utilizing the PCB transducer. Figure 3-20, shows the ratio between a run without ESD events and a run with ESD events, Run 1 and Run 2 respectively. A significant variation in pressure was observed near the ESD events. The $P_{rms}$ and $P'$ for this ratio was calculated to be 1.028 and 0.331, respectively. This indicated that there was a significant pressure variation during the ESD events, however it was much smaller than the pressure fluctuation in the static pressure transducer.
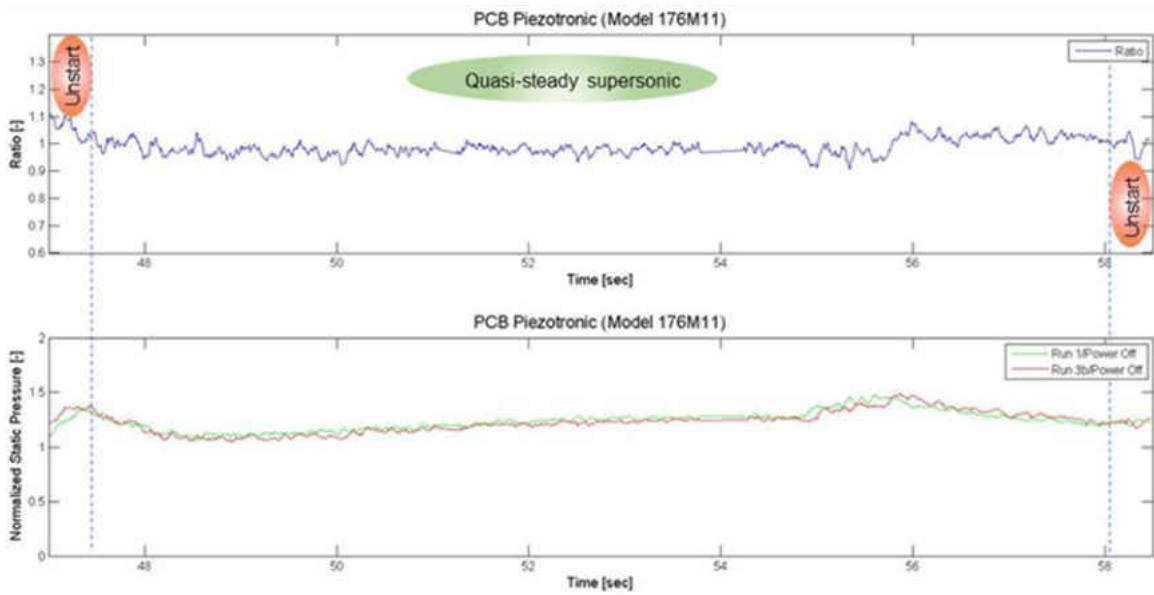
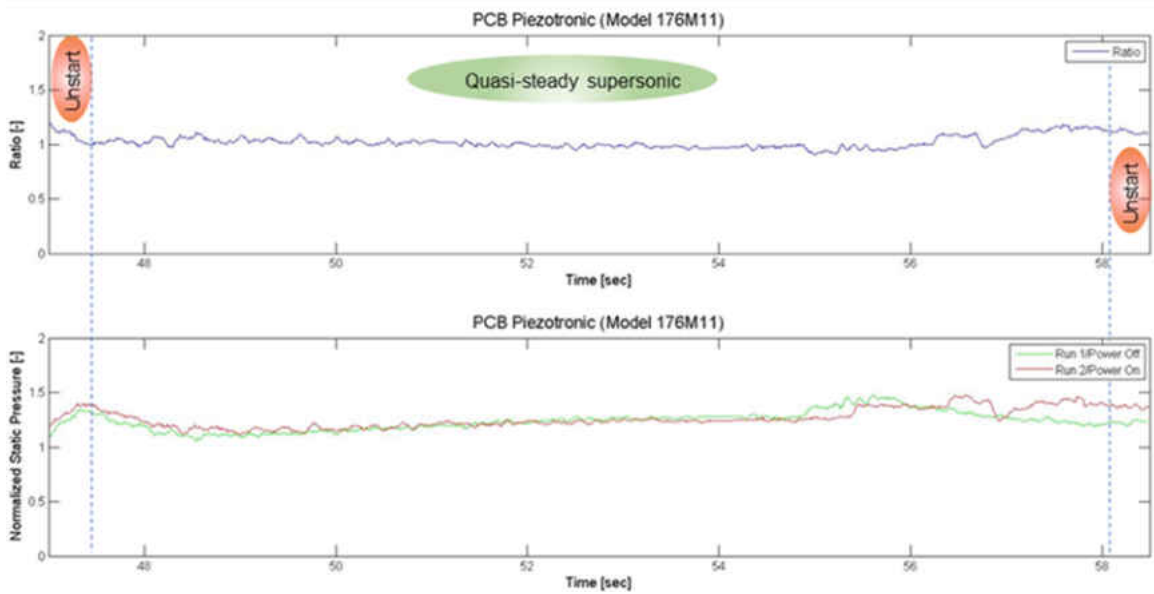**Figure 3-19: Ratio of Dynamic Pressure Measurements of Test without Sparks**



**Figure 3-20: Ratio of Dynamic Pressure Measurements of Test with Sparks**

3.3.1.2 Pressure Ratio Error Calculations

It was observed that the ESD event caused shock waves strong enough to affect the pressure measurements from these commonly used pressure transducers. This data allows for an order of magnitude comparison between the measured pressure and the pressure fluctuations seen from an ESD event. Table 3-3, outlines the results discussed in the previous section.

**Table 3-3: Pressure Ratio Error Calculations**

| Transducer/Sensor | Experiment | Comparison | Calculations |
|---|---|---|---|
| SensorTechnics | No ESD events | Run 3b/ Run 1 | P3b/1 = 1.004 ± 7.8% [-] |
| | ESD events | Run 2/ Run 1 | P2/1rms = 0.854 [-] |
| | | | P'2/1= 1.873 [-] |
| PCB Piezotronic | No ESD events | Run 3b/ Run 1 | P3b/1 = 1.004 ± 4.9% [-] |
| | ESD events | Run 2/ Run 1 | P2/1rms = 1.028 [-] |
| | | | P'2/1= 0.331 [-] |

The primary mechanism that affects the pressure measurement were spherical shock waves that emanated from the ESD event. The ESD event occurs close enough to the pressure port that the moving shock wave caused a transient change in pressure at the port. This is a well know characteristic of moving shock waves. Presumably the second mechanism was a change in thermal and EM filed that occurs from the ESD event.

This investigation highlights the sensitivity of static pressure measurements to ESD events in an environment encountered by aerospace vehicles. It sets a base for future work and empirical correlations that would help correct pressure data gathered by static pressure transducers exposed to ESD events.

### 3.3.1.3 Plotted Data Points

Figure 3-21, shows the data points that were gathered from Run 2. The static pressure for the ESD events was around 50-60 Torr before the ESD event caused fluctuation in the pressure trace. The gap height was set at 1.3 cm and the Mach number in the gap was estimated to be 1.65. Based on the measurement technique, a fluctuation of ±0.1 can be expected on the Mach number within the gap. These data points showed good agreement with the theoretical Paschen's Law model with compressible dynamic pressure term and Mach number term.

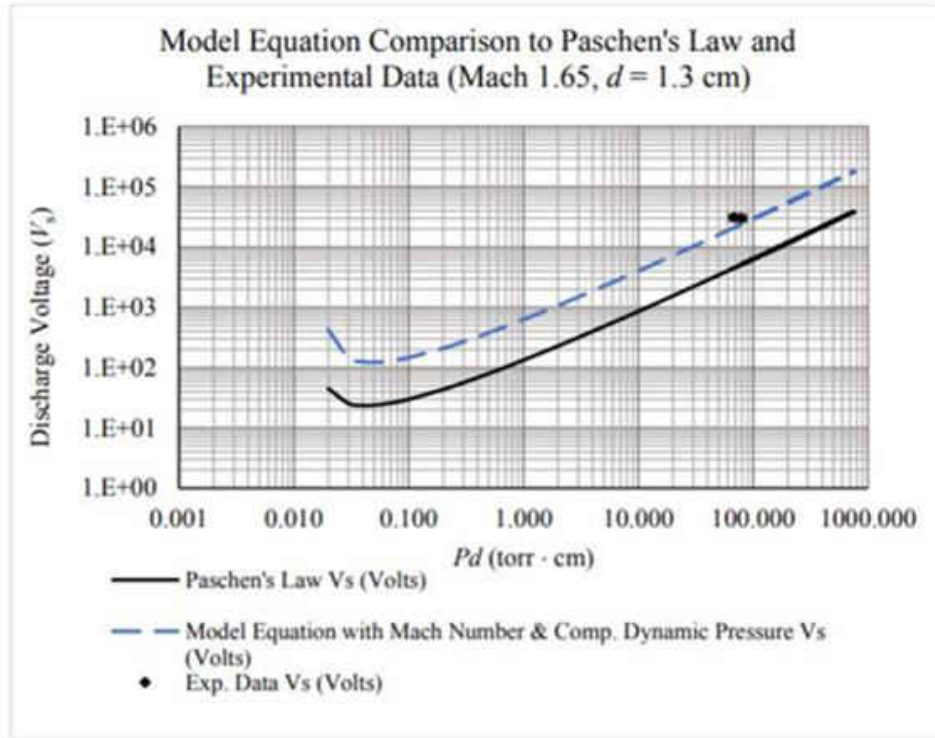**Figure 3-21: Experimental Data Plotted over Model Paschen's Law and Classical Paschen's Law**

Source: Hogue, Michael, D., Cox, Rachel, E, Mulligan, Jaysen, Kapat, Jayanta, Ahmed, Kareem, Cox, Rachel, E., Wilson, Jennifer, G., and Calle, Luz, M. "Revision of Paschen's Law Relating to the ESD of Aerospace Vehicle Surfaces" Proc. 2017 Electrostatic Joint Conference, University of Ottawa, June 13-15, 2017.

## 3.4    <u>Summary</u>

The final electrode design that was discussed in Chapter One was used to conduct the supersonic flow test described in this chapter. A schlieren imaging system was used to observe the shockwave and Mach waves, which provided for confirmation that supersonic flow had been established in the gap and the freestream Mach number calculations from the Mach wave angle. The pressure transducer was used measure the static pressure in the gap through a static pressure port on the ground wall of the electrode set up and a pressure sensor was used to measure the dynamic pressure in the test section. A high voltage power supply was used to charge the "hot" electrode. The data was recorded in a LabVIEW file and analyzed using MATLAB plotting and image processing tools.

Fluctuation in the static and dynamic pressure traces were noticed during the test. The magnitude of these fluctuations was quantified. For the static pressure sensor there the pressure ratio, $P_{rms}$ was 0.854 and the *P'* (maximum pressure difference over $P_{rms}$) was found to be *1.873*. The dynamic pressure sensor $P_{rms}$ was *1.028* and *P'* was *0.331*. The error associated with the dynamic pressure sensor was much smaller than the one associated with the static pressure sensor. However, this is not a definitive measure of the sensor accuracy due to the ESD event because the sensor locations were different and the ESD event discharge was prone to large variation. It was worthy to not that the all pressure fluctuations were brief and did not affect the over pressure measurements.

The run that successfully captured an ESD event in supersonic flow was set at *Mach 1.7* freestream which resulted in approximately *Mach 1.65* in the gap. The static pressure in the gap was measured to be between *50-60 Torr* during the ESD events. The gap separation height was set at *1.3 cm* for this test. The voltage prescribed on the "hot" electrode was *35kV* at *1.5 mA*. The data showed good

agreement with the theoretical Paschen's law model that accounts for a compressible dynamic

pressure and Mach number term.

# APPENDIX A: COPYRIGHT PERMISSIONS

**AIAA**
*Shaping the Future of Aerospace*

Search

Events    Publications    Membership & Communities    Careers    Continuing Education    Public Policy    About AIAA

American Institute of Aeronautics and Astronautics

Home   Publications

# Copyright & Permissions

## Author Copyright Assignment

- Transferring Copyright to AIAA
- Granting AIAA a License to Publish
- U.S. Government Authors and Contractors
- Authors Employed by Foreign Governments
- Choosing Copyright Options for Publication by AIAA

## Reuse Permissions

- Author Reuse Rights and Posting Policy
- Funding Agency Mandates and Open Access
- Data Mining of Text
- How to Request Permission to Reprint from AIAA

## Author Copyright Assignment

*Transferring Copyright to AIAA*

U.S. copyright law gives the copyright of a work to the person who wrote it. The American Institute of Aeronautics and Astronautics prefers to hold the copyright of any work it publishes with the clear understanding that the author and the author's organization or employer have the right to reproduce or adapt the work for their own purposes, provided that reproductions are not for sale. By owning the copyright, AIAA as a publisher is better able to maintain and protect the work and defend against improper use. AIAA does not claim any patent, trademark, or proprietary rights other than copyright.

When copyright is transferred to AIAA, examples of permitted uses retained by authors or their employers include incorporating material into lecture and in-house training materials and presentations, and posting accepted manuscripts of conference papers and journal articles on a personal website or in an institutional or government archive. Refer to AIAA's Self-Archiving and Posting Policy for details. In all cases copyright ownership by AIAA should be acknowledged and the AIAA published version, which is considered the version of record (VOR), should be cited. Links to the VOR in AIAA's electronic library, Aerospace Research Central (ARC), should be maintained, as appropriate.

### Authors Employed by Foreign Governments

In the case of works created by authors employed by *foreign (non–U.S.) governments*, these works frequently remain subject to foreign government or crown-owned copyright. AIAA will require a non-exclusive license to publish the work and use it for all current and future print and electronic uses.
Back to Top

### Choosing Copyright Options for Publication by AIAA

Options for copyright transfer or licensing of content are made available to authors of AIAA conference papers, journal articles, and contributed book chapters during the manuscript submission process. All authors and/or authorized individuals must assert that the manuscript is cleared for release, if required; acknowledge the originality and publication status of the work; and grant copyright or a license for AIAA's use of the material.

An explanation of the submission requirements and copyright options available to authors can be found here.

AIAA cannot advise authors on whether their work is within or outside the scope of their official duties, nor can AIAA advise coauthors with different employers how to determine copyright ownership and appropriate transfer or license.
Back to Top

## Reuse Permissions

### Author Reuse Rights and Posting Policy

Transfer of copyright to AIAA does not prevent authors from reproducing or adapting their work, in whole or in part, for their own *private use*, including for educational purposes, provided the material is not systematically reproduced or distributed and is not for sale.

In most cases, authors will be automatically granted permission by AIAA to reprint their own material in subsequent works, to include figures, tables, and verbatim portions of text, upon request. Explicit permission should be sought from AIAA through Copyright Clearance Center, as described below; all reprinted material must be acknowledged and the original source cited in full.

See also AIAA's Self-Archiving and Posting Policy, which addresses posting the accepted manuscript version on private websites and in institutional archives.

AIAA has no copyright claim on material in the public domain or owned by individuals, institutions, or foreign governments.
Back to Top

# REFERENCES

Cross, Jean A. Electrostatics: principles, problems and applications. Adam Hilger, 1987.

Hogue, Michael, D, Carlos, Calle, ESPL Report, "Electrostatic Evaluation of the ARES I FTS Antenna Materials", ESPLTR10-002, August 27, 2010. NASA, Kennedy Space Center.

Settles, G. S. "Specialized Schlieren Techniques." Schlieren and Shadowgraph Techniques (2001): 111-41. Web. 19 July 2016.

Sergey, Leonov, Dmitry, Yarantsev , Alexander, Kuriachy, and Victor, Soloviev. "Supersonic/Transonic Flow Control By Electro-Discharge Plasma Technique" 25th International Congress Of The Aeronautical Sciences, Hamburg, Germany, Sept. 3-8, 2006.

Nishihara, Munetake, Keisuke Takashima, Joseph Rich, and Igor Adamovich. "Mach 5 Bow Shock Control by a Nanosecond Pulse Surface DBD." 49th AIAA Aerospace Sciences Meeting including the New Horizons Forum and Aerospace Exposition (2011): n. pag. Web.

D. Knight, "Survey of Aerodynamic Drag Reduction at High Speed by Energy Deposition", Journal of Propulsion and Power, vol. 24, no. 6, p. 1153–1167, 2008.

Leonov, Sergey B., Jiachun Li, and Song Fu. "Review of Plasma-Based Methods for High-Speed Flow Control." (2011): n. pag. Web.

Leonov, Sergey B., Igor V. Adamovich, and Victor R. Soloviev, Dynamics of Near-surface Electric Discharges and Mechanisms of Their Interaction with the Airflow (n.d.): n. pag. Web. 19 Aug. 2016.

Leonov, S., D. Yarantsev, and F. Falempin. "Flow Control in a Supersonic Inlet Model by Electrical Discharge." Progress in Flight Physics (2012): n. pag. Web. 19 Aug. 2016.

S. Leonov, D. Yarantsev, A. Kuriachy and V. Soloviev, "Supersonic/Transonic Flow Control By ElectroDischarge Plasma Technique", in Proceedings of 25th International Congress of the Aeronautical Sciences (ICAS), Paper ICAS-2006-2.11.1, Hamburg, Germany, 3-8 September 2006.

N. Benard and E. Moreau, "Electrical and mechanical characteristics of surface AC dielectric barrier discharge plasma actuators applied to airflow control", Experiments in Fluids, vol. 55, p. 1846, 2014.

D. Caruana, "Plasmas for aerodynamic control", Plasma Phys. Control. Fusion, vol. 52, p. 124045, 2010.

J.-J. Wang, K.-S. Choi, L.-H. Feng, N. Jukes and D. Whalley, "Recent developments in DBD plasma flow control", Prog. Aerospace Sci., vol. 62, pp. 52-78, 2013.

T. Jukes, K.-S. Choi, G. Johnson and S. Scott, "Turbulent Boundary-Layer Control for Drag Reduction Using Surface Plasma", in 2nd AIAA Flow Control Conference, AIAA Paper 2004-2216, 28 June - 1 July 2004, Portland, OR, USA, 2004.

S. Merriman, E. Plonjes and P. Palm, " Shock wave control by nonequilibrium plasmas in cold supersonic gas flows", AIAA Journal, vol. 39, pp. 1547-1552, 2001.

Reichenbach, H. "Contributions of Ernst Mach to Fluid Mechanics." Annual Review Fluid Mechanics, 1983, pp. 1–29., Accessed 1 Mar. 2017.

Hogue, Michael, D., Kapat, Jayanta, Ahmed, Kareem, Cox, Rachel, E., Wilson, Jennifer, G., Calle, Luz, M., and Mulligan, Jaysen. "Dynamic Gas Flow Effects on the ESD of Aerospace Vehicle Surfaces" *Proc. 2016 Electrostatic Joint Conference, Purdue Univeristy, June 13-16, 2016*.

Friedrich Paschen "Ueber die zum Funkenübergang in Luft, Wasserstoff und Kohlensäure bei verschiedenen Drucken erforderliche Potentialdifferenz

A. Von Hippel, Molecular Science and Molecular Engineering, (MIT Press, Wiley & Sons, 1959), pp 39-47.

Anderson, John David. Modern compressible flow: with historical perspective. McGraw-Hill, 2007.

Sultanian, Bijay, Fluid Mechanics: An Intermediate Approach, N.P.: CRC, n.d. Print, p. 33.

Hogue, Michael, D., Cox, Rachel, E, Mulligan, Jaysen, Kapat, Jayanta, Ahmed, Kareem, Cox, Rachel, E., Wilson, Jennifer, G., and Calle, Luz, M. "Revision of Paschen's Law Relating to the ESD of Aerospace Vehicle Surfaces" *Proc. 2017 Electrostatic Joint Conference, University of Ottawa, June 13-15, 2017*.

R. W. Fox, A. T. McDonald, Introduction to Fluid Mechanics, 2nd ed., John Wiley & Sons, 1978, p. 496

Bell, J. H., and R. D. Mehta. "Contraction design for small low-Speed wind tunnels." National Aeronautics and Space Administration, Contraction design for small low-Speed wind tunnels, 1988.

Ben-Dor, Gabi. Shock wave reflection phenomena. Springer, 2007.